PAPER • OPEN ACCESS

Macroscopic coherence as an emergent property in molecular nanotubes

To cite this article: Marco Gullì *et al* 2019 *New J. Phys.* **21** 013019

View the article online for updates and enhancements.

New Journal of Physics

The open access journal at the forefront of physics

CrossMark

PAPER

Macroscopic coherence as an emergent property in molecular nanotubes

Marco Gullì[1], Alessia Valzelli[1], Francesco Mattiotti[1,2], Mattia Angeli[1,3], Fausto Borgonovi[1,2] and Giuseppe Luca Celardo[4]

[1] Dipartimento di Matematica e Fisica and Interdisciplinary Laboratories for Advanced Materials Physics, Università Cattolica del Sacro Cuore, via Musei 41, I-25121, Brescia, Italy
[2] Istituto Nazionale di Fisica Nucleare, Sezione di Pavia, via Bassi 6, I-27100, Pavia, Italy
[3] International School for Advanced Studies (SISSA), Via Bonomea 265, I-34136, Trieste, Italy
[4] Benemérita Universidad Autónoma de Puebla, Apartado Postal J-48, Instituto de Física, 72570, Mexico

E-mail: nicedirac@gmail.com

Abstract

Nanotubular molecular self-aggregates are characterized by a high degree of symmetry and they are fundamental systems for light-harvesting and energy transport. While coherent effects are thought to be at the basis of their high efficiency, the relationship between structure, coherence and functionality is still an open problem. We analyse natural nanotubes present in Green Sulphur Bacteria. We show that they have the ability to support macroscopic coherent states, i.e. delocalized excitonic states coherently spread over many molecules, even at room temperature. Specifically, assuming a canonical thermal state we find, in natural structures, a large thermal coherence length, of the order of 1000 molecules. By comparing natural structures with other mathematical models, we show that this macroscopic coherence cannot be explained either by the magnitude of the nearest-neighbour coupling between the molecules, which would induce a thermal coherence length of the order of 10 molecules, nor by the presence of long-range interactions between the molecules. Indeed we prove that the existence of macroscopic coherent states is an emergent property of such structures due to the interplay between geometry and cooperativity (superradiance and super-transfer). In order to prove that, we give evidence that the lowest part of the spectrum of natural systems is determined by a cooperatively enhanced coupling (super-transfer) between the eigenstates of modular sub-units of the whole structure. Due to this enhanced coupling strength, the density of states is lowered close to the ground state, thus boosting the thermal coherence length. As a striking consequence of the lower density of states, an energy gap between the excitonic ground state and the first excited state emerges. Such energy gap increases with the length of the nanotube (instead of decreasing as one would expect), up to a critical system size which is close to the length of the natural complexes considered.

1. Introduction

Coherent effects, as fragile as they may seem, might be able to survive in complex systems even in presence of strong noise induced by the coupling to an external environment. They are often related to functions in complex chemical and biophysical systems [1–3]. Understanding under which conditions robust coherent effects can be sustained even at room temperature is a central issue for designing efficient quantum devices.

Molecular nanotubes are among the most interesting and most investigated structures. They are present in several natural photosynthetic complexes, for instance in the Green Sulphur Bacteria [4–11] or in Phycobilisome Antennas [12–15]. They are also present in other biomolecular systems, for instance in Microtubules, which are fundamental biological structures, showing interesting similarities with photosynthetic Antenna complexes [16, 17]. Also artificial molecular nanotubes are at the centre of research interest [18–21]. Nanotubular molecular aggregates are extremely efficient for light-harvesting and energy transport and they present a very ordered

structure with a high degree of symmetry [6–8, 22–25]. The high degree of symmetry concerns both the molecule positions and the orientation of their transition dipoles. Despite all that, a clear understanding of how structural features in molecular aggregates can sustain coherent effects and explain their high efficiency is still missing.

Some of the primary coherent effects which are thought to be responsible for the high efficiency of molecular nanotubes are induced by the delocalization of the excitation over many molecules. Since the sunlight is very dilute, usually only one excitation is present in such complexes, so that single-excitation delocalized states are usually investigated. Delocalized excitonic states can lead to cooperative effects, such as superradiance [9, 10, 22, 26–29] and super-transfer [30, 31], and they can be useful in both natural or artificial light-harvesting complexes [19, 28, 32–43]. Specifically, coherently delocalized excitonic states can have a large dipole strength which strongly couples them to the electromagnetic field (EMF). Thus, these states are able to super-absorb light at a rate much larger than the single-molecule absorbing rate, since the absorption rate of delocalized excitonic states can increase with the number of molecules over which the excitation is delocalized [9, 10]. States with a large dipole strength can also couple between themselves efficiently, inducing a super-transfer coupling between distant molecular aggregates [31] or different parts of the same aggregate as we show here. Delocalized single excitonic states over a large number of molecules are called macroscopic coherent states and they are studied both for applications and basic science [44–50].

Molecular nanotubes are composed by a network of self-assembled photo-active molecules. Each molecule can be treated as a two level system, characterized by both an excitation energy and a transition dipole moment which determines its coupling with the EMF and with the other molecules. The interaction between the molecules is often assumed to be dipole–dipole [22–25] which decays with the distance as $1/r^3$ or, in some approximate scheme, as nearest-neighbour (NN) [21] only. While the results thus obtained are certainly very interesting, care is needed to use such simplifications in large molecular structures. Indeed, dipole–dipole interaction is valid when the distance between the molecules is sufficiently large and the overall system size L is considerably smaller than the wavelength λ_0 connected with the excitation energy of the molecules (small volume limit). Since nanotubular aggregates can be large, here we consider a more accurate Hamiltonian interaction [51] which takes into account the interaction between oscillating charges in each molecule. Such description reduces to the usual dipole–dipole interaction in the small volume limit.

Using such radiative Hamiltonian, we have analysed the existence of macroscopic coherent states at room temperature in different, natural and artificial, molecular nonotubes. Since the molecules in such structures are tightly packed, their interaction energy can be strong, of the order of several times $k_B T \approx 200$ cm^{-1} with $T = 300$ K. Such strong interaction is thought to be able to support excitonic delocalization even at room temperature. While for small molecular aggregates, the existence of a large coupling compared to $k_B T$ can explain the existence of delocalized excitonic states even at room temperature., for large molecular aggregates, usually the mean level spacing between the states is very small and many states are mixed by the external environmental noise. For instance, at thermal equilibrium all the states between the ground state and $k_B T$ are incoherently mixed. This argument seems to suggest that in large aggregates it is very difficult to have large coherence lengths. Nevertheless here we show that the symmetric arrangement of the molecules is able to induce excitonic delocalization at room temperature well beyond what one could expect from the magnitude of the NN coupling between the molecules. Moreover, by comparing natural structures with few mathematical models of self-aggregated molecular nanotubes we show that the degree of macroscopic coherence cannot be explained even by the long-range nature of the coupling between the molecules. We connect such enhanced delocalization to the super-transfer coupling present inside such structures, which decreases the density of states in the low energy region of the spectrum, thus increasing the mean level spacings between the excitonic eigenstates. Thus our main result is that macroscopic coherence in natural molecular nanotubes is an emergent property produced by specific cooperative effects which cannot be reduced either to the range of the interaction or to the magnitude of the coupling between the molecules. The presence of a large coherence length at room temperature in molecular nanotubes suggests the possibility that such structures can exploit superabsorption of light and supertransfer of excitation for efficient light-harvesting and energy transport. Superabsorption, induced by giant dipoles, can enhance the absorption rate of sun-light [30, 52] while supertransfer can enhance the diffusion coefficient for energy transfer [31]. Both such effects induced by excitonic delocalization are thought to play an important role in natural photosynthetic complexes [4, 30, 31, 52].

Specifically, in this paper we investigate the *Chlorobium Tepidum* Antenna complexes of Green Sulphur bacteria. Green Sulphur bacteria are photosynthetic organisms which live in deep water where the sunlight flux is very low [5] and they are among the most efficient photosynthetic systems [6–8]. Similarly to other antenna complexes present in nature [12–15], they present a high degree of symmetry being arranged in nontrivial cylindrical structures with an ordered orientation of the molecule dipoles. We analyse both the wild type (WT) and the triple mutant type (MT), which have been recently investigated in [53, 54].

Understanding the connection between functionality and structure in such complexes will enhance our comprehension of natural photosynthesis and it could also inspire efficient bio-mimetic devices for energy

transport and light-harvesting. The mechanism described in this paper, which allows large molecular aggregates to sustain macroscopic coherent states even at room temperature, could inspire the design of efficient engineered nano-structures.

In sections 2 and 3 we present the cylindrical models studied. In section 4.1 the existence of a delocalized SRS close to the ground state for the natural models is shown. In sections 4.2 and 4.3 the thermal coherence length is introduced and analysed. Natural complexes are shown to be able to support the largest thermal coherence length with respect to the other models considered. The evidence produced in these sections allows to conclude that the large thermal coherence length of natural aggregates cannot be explained by the magnitude of the coupling or by the range of the interaction between the molecules. In section 5 we explain that the origin of such macroscopic coherent states found in natural complexes lies in their specific geometry which induces a supertransfer coupling inside the complexes. Such supertansfer coupling strongly affects the lowest part of the spectrum thus enhancing the thermal coherence length. In section 6, we analyse structures which are more complex than single cylindrical surfaces. Specifically, we consider tubular structures made of four concentric cylindrical surfaces, as they appear in natural antenna complexes of Green Sulphur bacteria [53–56]. We show that these structures display an enhanced delocalization of the excitation with respect to single cylindrical surfaces. Finally in section 7 we give our conclusions and perspectives.

2. The models

The natural Antenna complexes present in Green Sulphur bacteria have lengths of 1000–2000 Å, widths of 100–600 Å and they can contain a number of molecules between 50 000 and 250 000, typically arranged into concentric cylindrical surfaces [5, 57]. It is important to remark that, depending on the environment and on the growing conditions [58], some samples could show an alternation between tubular aggregates and non-tubular curved lamellae [59, 60]. Nevertheless, in spite of the heterogeneity of the structures experimentally observed, we will consider here cylindrical surfaces only with a radius of 6 nm and length up to $L = 232$ nm composed of 16800 molecules.
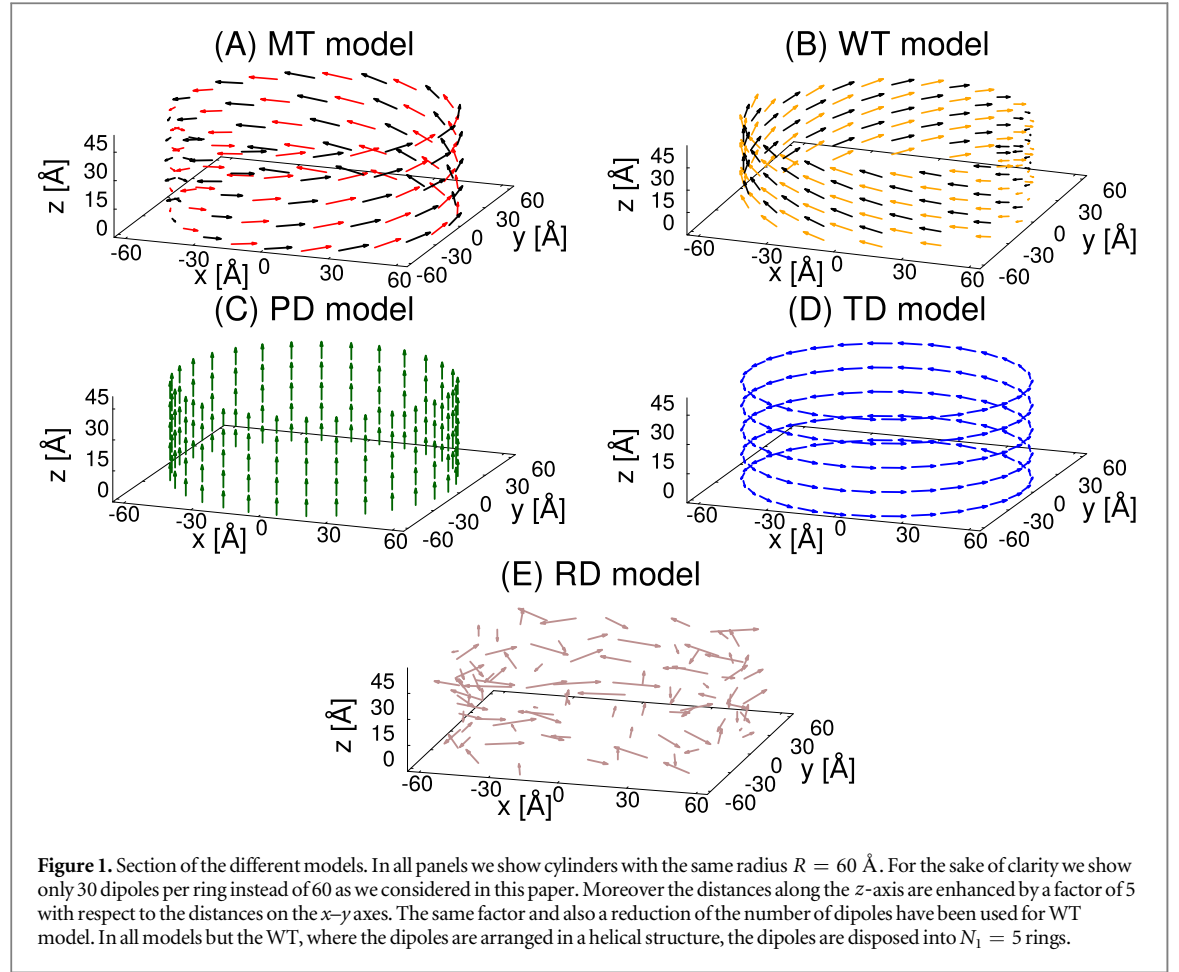
Specifically, we analyse five different cylindrical models with fixed radius ($R = 60$ Å) and total number of chromophores N. These models differ for the geometrical arrangement of the chromophores along the cylindrical surface. In details they are:

- *Chlorobium Tepidum* bchQRU triple mutant (MT),

- *Chlorobium Tepidum* wild type (WT),

- parallel dipoles cylinder (PD),

- tangent dipoles cylinder (TD),

- random dipoles cylinder (RD).

While the first two are representative of natural systems, the others are mathematical models with a suitable symmetric arrangements of chromophores (TD and PD) while the last one (RD) is characterized by a random orientation of the dipole moments. The molecule positions and dipole orientations for the natural models have been taken from literature [53, 54, 56] and they correspond to the values capable to reproduce experimental results.

A schematic view of the arrangement of the dipoles on the cylindrical surfaces for all models is shown in figure 1, while all other technical details can be found in appendix A. Notice that all the models but the WT share the same basic structure: the cylinder is made by a collection of N_1 rings composed of $N_2 = 60$ molecules equally spaced on each ring. The difference between the different models lies mainly in the dipole orientation, while the positions of the dipoles are the same in all models apart from an angular twist between rings in the MT:

- PD model: all dipoles are oriented parallel to the z axis

- TD model: all dipoles are perpendicular to the z direction and tangential to the cylindrical surface

- MT model: here the dipoles have a fixed z component, but also a component perpendicular to the z direction, see appendix A for details. Note that the component perpendicular to the z direction points inward and outward alternatively with respect to the plane tangent to the cylindrical surface with a small angle α (see black and red arrows in figure 1(A)).

- RD model: the position of the dipoles is the same of the PD and TD models but the orientation of the dipoles is fully random on the unit sphere.

Figure 1. Section of the different models. In all panels we show cylinders with the same radius $R = 60$ Å. For the sake of clarity we show only 30 dipoles per ring instead of 60 as we considered in this paper. Moreover the distances along the z-axis are enhanced by a factor of 5 with respect to the distances on the x–y axes. The same factor and also a reduction of the number of dipoles have been used for WT model. In all models but the WT, where the dipoles are arranged in a helical structure, the dipoles are disposed into $N_1 = 5$ rings.

On the other hand the WT model, see figure 1(B), is not composed of separated rings but instead it is arranged in a complicated helical structure, see appendix A for details.

3. The Hamiltonian and the dipole approximation

Each molecule is represented as a two-level system with an excitation energy e_0 and a transition dipole moment $\vec{\mu}$. The parameters of the aggregates considered here have been taken from literature [61, 62] to be the ones characterizing the Antenna Complexes in Green Sulphur bacteria. Specifically we set for the excitation energy of all the molecules $e_0 = 15390$ cm^{-1} [62], corresponding to $\lambda_0 \approx 650$ nm, so that

- $k_0 = 2\pi e_0 \times 10^{-8} = 9.670 \times 10^{-4}$ Å^{-1}.

- $\mu = \sqrt{30}$ D [61] so that $|\mu|^2 = 151024$ Å^3 cm^{-1} (for the conversion, see[5]).

- $\gamma = 4|\mu|^2 k_0^3/3 = 1.821 \times 10^{-4}$ cm^{-1}, corresponding to the radiative lifetime $\tau_\gamma = 29.15$ ns (for the conversion, see[6]).

Choosing the basis states in the single excitation manifold, where the state $|i\rangle$ refers to a state in which the ith molecule is excited while all the others are in the ground state, the nanotubes can be described through a

---

[5] Let us recall that, in Gaussian units, the unit dipole–dipole interaction energy is $[E] = [\mu]^2 [d]^{-3}$, where $[\mu]$ is the unit dipole and $[d]$ the unit distance. We express the dipoles in D (Debye), the distance in Å and the energy in cm^{-1} units (applying the standard conversion $[E]/(hc)$, with h being the Planck constant and c the speed of light), so that $[\mu]^2/(hc) = $ cm^{-1} Å^3. Now, from the definition of Debye we have $1 D = 10^{-18}$ cm$^{5/2}$ g$^{1/2}$ s^{-1} from which $1 D^2 = 10^{-12}$ cm^2 gs^{-2} Å^3. Recalling the Planck constant $h = 6.626 \times 10^{-27}$ cm^2 g s^{-1} and the speed of light $c \simeq 2.998 \times 10^{10}$ cm s^{-1}, we have $1 D^2/(hc) \simeq 5034$ cm^{-1} Å^3. So, a transition dipole $\mu = \sqrt{30} D$ results in $|\mu|^2 = 30 \times 5034$ cm^{-1} Å$^3 \simeq 151020$ cm^{-1} Å^3. Note that in these calculations we write explicitly where the energy is divided by hc for clarity, while in the main text we always assume implicitly that any energy is divided by hc.

[6] The lifetime related to an energy width γ is defined as $\tau_\gamma = \hbar/\gamma$. Note that we implicitly divide each energy by hc (with h being the Planck constant and c the speed of light), so that $[\gamma]/(hc) = $ (cm)$^{-1}$. Therefore, the unit time is $[\tau_\gamma] = \frac{h}{2\pi[\gamma]} = (2\pi c (\text{cm})^{-1})^{-1}$, where $c \simeq 2.998 \times 10^{-2}$ cm ps^{-1}. Thus, given a width in (cm)$^{-1}$ units, its lifetime is obtained by multiplying the width by $2\pi c \simeq 0.1884$ cm ps^{-1} and taking the reciprocal of the result.

non-Hermitian Hamiltonian which takes into account the interaction between the molecules mediated by the EMF. The effective Non-Hermitian Hamiltonian (also called radiative Hamiltonian) is commonly used to model the interaction with the EMF in different systems, such as natural light-harvesting complexes [51, 63] and cold atomic clouds [64]. The radiative Hamiltonian has been derived by many authors, see for instance [63, 65], and it is accurate when the intensity of the EMF is weak so that the single excitation approximation is valid. Such approximation is extremely good for sunlight absorption since sunlight is very diluted. The radiative Hamiltonian reads:

$$H = \sum_{i=1}^{N} e_0 |i\rangle \langle i| + \sum_{i \neq j} \Delta_{ij} |i\rangle \langle j| - \frac{i}{2} \sum_{i,j=1}^{N} Q_{ij} |i\rangle \langle j|. \tag{1}$$

The terms Δ_{ij} and Q_{ij} derive from the interaction with the EMF. The real and imaginary diagonal parts of the intermolecular coupling are given respectively by

$$\Delta_{nn} = 0, \quad Q_{nn} = \frac{4}{3}\mu^2 k_0^3 = \gamma, \tag{2}$$

with $\mu = |\vec{\mu}|$ being the transition dipole, while the off-diagonal terms ($n \neq m$) by

$$\Delta_{nm} = \frac{3\gamma}{4}\left[\left(-\frac{\cos(k_0 r_{nm})}{(k_0 r_{nm})} + \frac{\sin(k_0 r_{nm})}{(k_0 r_{nm})^2} + \frac{\cos(k_0 r_{nm})}{(k_0 r_{nm})^3}\right)\hat{\mu}_n \cdot \hat{\mu}_m \right.$$
$$\left. - \left(-\frac{\cos(k_0 r_{nm})}{(k_0 r_{nm})} + 3\frac{\sin(k_0 r_{nm})}{(k_0 r_{nm})^2} + 3\frac{\cos(k_0 r_{nm})}{(k_0 r_{nm})^3}\right)(\hat{\mu}_n \cdot \hat{r}_{nm})(\hat{\mu}_m \cdot \hat{r}_{nm})\right], \tag{3}$$

$$Q_{nm} = \frac{3\gamma}{2}\left[\left(\frac{\sin(k_0 r_{nm})}{(k_0 r_{nm})} + \frac{\cos(k_0 r_{nm})}{(k_0 r_{nm})^2} - \frac{\sin(k_0 r_{nm})}{(k_0 r_{nm})^3}\right)\hat{\mu}_n \cdot \hat{\mu}_m \right.$$
$$\left. - \left(\frac{\sin(k_0 r_{nm})}{(k_0 r_{nm})} + 3\frac{\cos(k_0 r_{nm})}{(k_0 r_{nm})^2} - 3\frac{\sin(k_0 r_{nm})}{(k_0 r_{nm})^3}\right)(\hat{\mu}_n \cdot \hat{r}_{nm})(\hat{\mu}_m \cdot \hat{r}_{nm})\right], \tag{4}$$

where $\hat{\mu}_n := \vec{\mu}_n / \mu$ is the unit dipole moment of the nth site and $\hat{r}_{nm} := \vec{r}_{nm}/r_{nm}$ is the unit vector joining the nth and the mth sites.

Diagonalizing the Hamiltonian (1) we obtain the complex eigenvalues $\varepsilon_n = E_n - i\frac{\Gamma_n}{2}$ where Γ_n is the radiative decay of the nth eigenstate. In general it differs from the radiative decay of the single molecule γ. In particular, when the ratio $\Gamma_n/\gamma \gg 1$ we will talk about a superradiant state (SRS), otherwise when $\Gamma_n/\gamma \ll 1$ the state is called 'subradiant'. In other words, a SRS can radiate much faster than a single molecule, while a subradiant one radiates at a rate much slower than the single molecule radiative decay.

Within the range of parameters considered here, the imaginary part Q_{ij} can be considered a small perturbation of the real part of the Hamiltonian (1), moreover the system size is small compared to the wavelength associated with the optical transition of the molecules (the maximal size considered here is $L/\lambda_0 \approx 0.4$). In such case, the optical absorption of an eigenstate of the aggregate can be estimated in terms of its dipole strength, computed only from the real part of the Hamiltonian (1). Denoting the nth eigenstate of the real part of the Hamiltonian (1) with $|E_n\rangle$, we can expand it on the site basis, so that

$$|E_n\rangle = \sum_{i=1}^{N} C_{ni}\,|i\rangle. \tag{5}$$

Note that the site basis is referred to the molecules and is composed by the states $|i\rangle$, each of them carrying a dipole moment $\vec{\mu}_i$. If N is the total number of molecules, then we will express the transition dipole moment $\vec{D}_n$ associated with the nth eigenstate as follows:

$$\vec{D}_n = \sum_{i=1}^{N} C_{ni}\,\hat{\mu}_i. \tag{6}$$

The dipole strength of the nth eigenstate is defined by $|\vec{D}_n|^2$ (note that due to normalization $\sum_{n=1}^{N}|\vec{D}_n|^2 = N$). Under the approximation that the imaginary part of the Hamiltonian (1) can be treated as a perturbation and $L/\lambda_0 \ll 1$ we have $|\vec{D}_n|^2 \approx \Gamma_n/\gamma$, which is valid for states with a large radiative decay rate (see appendix B for a comparison between dipole strengths and radiative decay widths for all models).

Thus, in the following we will consider only the real part of the Hamiltonian (1):

$$H_r = \sum_{i=1}^{N} e_0 |i\rangle \langle i| + \sum_{i \neq j} \Delta_{ij} |i\rangle \langle j|. \tag{7}$$

where $\Delta_{i,j}$ is given in equation (3).

Finally we note that for small systems, when $k_0 r_{ij} \ll 1$, the Hamiltonian (1) becomes

$$Q_{ij} \simeq \gamma \hat{\mu}_i \cdot \hat{\mu}_j,$$

$$\Delta_{ij} \simeq \frac{\vec{\mu}_i \cdot \vec{\mu}_j - 3(\vec{\mu}_i \cdot \hat{r}_{ij})(\vec{\mu}_j \cdot \hat{r}_{ij})}{r_{ij}^3}. \tag{8}$$

In this limit, the real term Δ_{ij} represents a dipole–dipole interaction energy with $\mu = |\vec{\mu}_j|$ and the radiative decay $\gamma = \frac{4}{3}|\mu|^2 k_0^3$. The dipole approximation is widely used in literature to model molecular aggregates which are small compared to the wavelength of the absorbed light. Nevertheless when the dimension of the aggregate becomes comparable with the wavelength λ_0 the dipole–dipole approximation fails. For the maximal sizes considered here ($L/\lambda_0 \approx 0.4$) the dipole approximation can be considered good, even if there are already non-negligible deviations in some quantities between the dipole–dipole interaction in equation (8) and the Hamiltonian in equation (7), see appendix C. For this reason in the following we will use the expression given in equation (7).

4. Single cylindrical structures: results

In this section we analyse first the collective dipole strengths of the eigenstates of the different models, showing the emergence of a SRS close to the ground state in natural complexes, see subsection 4.1. The coherence length is defined in subsection 4.2 where also a new model with only nearest-neighbour couplings is introduced. Finally in subsection 4.3 the results of our analysis about the thermal coherence length for the different models is shown.

4.1. Collective dipole strength
As a first goal let us analyse the dipole strengths associated with the eigenstates of the Hamiltonian models described in the previous section. For the five models introduced previously we diagonalized the Hamiltonian in equation (7), and we analysed in detail the dipole strengths $|D_n|^2$ of all eigenstates. In figures 2(A)–(E) we plot $|D_n|^2$ as a function of the energy $E_n - e_0$ of the corresponding eigenstate. All models but the random one (E) are characterized by the presence of SRSs in different positions of the energy spectrum. For instance for the MT model the state having the largest dipole strength is the ground state while for the WT model it is very close to it. Note that the position of the SRS is below the excitation energy of a single molecule. Since the dipole strength of the eigenstates determines the absorption spectrum [9, 10], a superradiant ground state implies a red-shifted absorption spectrum which is a typical behaviour for molecular J-aggregates [9, 10, 19, 22]. On the other hand for both the TD and PD models the SRSs are in the middle of the energy spectrum (C, D). Contrary to this general trend, the absence of ordering characterizing the random model (RD) does not guarantee the presence of SRSs. Indeed it is well known that in the small volume limit $L/\lambda \ll 1$ symmetry is necessary to preserve super- and sub-radiance [65].

This is a clear indication that natural structures tend to push the SRS to the lowest energy region. Moreover, as the comparison with the other symmetric structure shows, this is not a trivial consequence of the symmetric arrangement. Other symmetric arrangements, such as the TD and PD, are still characterized by SRS but 'living' in an energy region far from the ground state.

SRSs are typically characterized by a collective dipole strength which grows with the length of the cylindrical structure. This is clearly shown in figure 2(F) where the maximal dipole strength $|D_{\max}|^2$ is shown as a function of the length L of the cylinder. As one can see the maximal dipole strength grows $\propto L$ for all models but the random one for which it is independent of L.

4.2. Delocalized excitonic states at room temperature
Given a quantum state specified by the density matrix $\hat{\rho}$ it is possible to define its coherence length in the single excitation manifold defined by the basis states $|i\rangle$ [66, 67]:

$$L_\rho = \frac{1}{N} \frac{\left(\sum_{ij} |\rho_{ij}|\right)^2}{\sum_{ij} |\rho_{ij}|^2}. \tag{9}$$

The expression of L_ρ in equation (9) measures how much a single excitation is spread coherently over the molecules composing the aggregate. To give an idea of its physical meaning let us consider three different simple cases:

- a pure localized state, $\hat{\rho} = |i\rangle \langle i|$; then it is easy to see that the coherence length defined in equation (9) is given by $L_\rho = 1/N$. This case represents the minimal value that L_ρ can get.

Figure 2. (A)–(D) Squared dipole strength $|D_n|^2$ as a function of the energy $E_n - e_0$. Superradiance arises in all cylindrical models characterized by a high degree of geometrical symmetry. However, in the mathematical models made up of parallel and tangent dipoles (panels (C, D)) the SRS does not coincide definitely with the ground state, nor it is close to it. On the other hand, in the MT model (A) the ground state is superradiant while in the WT model (B) the SRS, even if it does not coincide with the ground state, it is indeed very close to it. In panels (A, B, C, D) insets are shown with a magnification of the energy spectrum close to the SRS. In the insets the arrows indicate the position of the ground state. (E) Average squared dipole strength $\langle |D_n|^2 \rangle$ as a function of the eigenstate index. The average has been computed over 10 disorder realizations. (F) $|D_{max}|^2$ as a function of the cylindrical length L. A linear dependence, as given by the dashed line $|D_{max}|^2 \propto L$, emerges clearly from all structures except the RD model (brown). Different colours stand for different models: MT (red), WT (orange), PD (green), TD (blue) and RD (brown). In panels (A–E) we considered cylindrical structures made of 6000 dipoles. In panel (F) we considered cylindrical structures with a number of dipoles varying from 60 to 6000.

- A completely delocalized mixed state characterized by the density matrix: $\hat{\rho} = (1/N) \sum_{i=1}^{N} |i\rangle \langle i|$. In this case we have $L_\rho = 1$. This state is maximally delocalized in the basis, but it is completely incoherent.

- Lastly we consider the fully delocalized coherent state: $\hat{\rho} = (1/N) \sum_{i,j=1}^{N} |i\rangle \langle j|$. In this case we have $L_\rho = N$. Note that any pure state with constant amplitude $1/\sqrt{N}$ over the sites and arbitrary phases would give the same result.

Generally speaking we can see that $1/N \leqslant L_\rho \leqslant N$. The closer L_ρ is to N, the higher a coherent delocalization can be assigned to our state. In the same way $L_\rho < 1$ indicates an incoherent localized state. States characterized by $L_\rho \sim 1$ have a little ambiguity (since both localization and coherence are measured on the same length scale).

In what follows we will consider the previous models of cylindrical structures and we will compare them with an additional model where the positions of the molecules are the same of the MT model, but their interaction is only NN. In this way we will be able to address the relevance of the range of the interaction to the thermal coherence length. For this purpose, let us consider a variant of the MT model, in which the Hamiltonian matrix elements are defined as follows:

$$H_{NN} = \begin{cases} \sum_{i=1}^{N} e_0 |i\rangle \langle i| + \sum_{i \neq j} \Delta_{ij} |i\rangle \langle j| & \text{if } r_{ij} \leqslant \bar{d}, \\ 0 & \text{if } r_{ij} > \bar{d} \end{cases} \tag{10}$$

where we have introduced the cut-off distance $\bar{d} = 9$ Å and $\Delta_{i,j}$ is defined in equation (3, 7). In other words any lattice point interacts only with its four nearest neighbours.

Table 1. Absolute value of the NN coupling for the different models. Ω_1: azimuthal coupling for NN sites in the same ring (or between two adjacent chains for the WT). Ω_2: vertical coupling for NN sites between rings (or in the same chain for the WT).

	Ω_1 (cm^{-1})	Ω_2 (cm^{-1})
MT	618	248
WT	115	629
PD	610	528
TD	1218	264

For all the models above we have computed the thermal coherence length at room temperature ($T = 300$ K), defined for a state at the canonical equilibrium and whose matrix elements are given by:

$$\rho_{ij} = \sum_n \frac{e^{-\beta E_n}}{\mathrm{Tr}(e^{-\beta \hat{H}})} \langle i | E_n \rangle \langle E_n | j \rangle, \tag{11}$$

where $\beta = 1/k_B T$. A very important question to be answered is how much the symmetrical arrangements that give rise to SRSs are also able to produce a large thermal coherence length at room temperature. Note that even if we consider the coherence length at thermal equilibrium, this does not mean that out-of-equilibrium processes are not important in molecular nanotubes. Indeed in [68] strong evidence of ultra-fast transport in natural structures with transfer times less than 100 fs have been discussed. Nevertheless thermal equilibrium can be considered as a worst case scenario for coherences, see also discussion in the conclusions. For this reason assuming thermal equilibrium can be considered a good starting point to assess the structural robustness of quantum coherence to thermal noise.

In that regard we calculate the coherence length L_ρ according to equation (9), using a thermal density matrix defined in equation (11), as a function of the cylindrical length L for each of the cylindrical models studied so far, including the NN model described by equation (10).
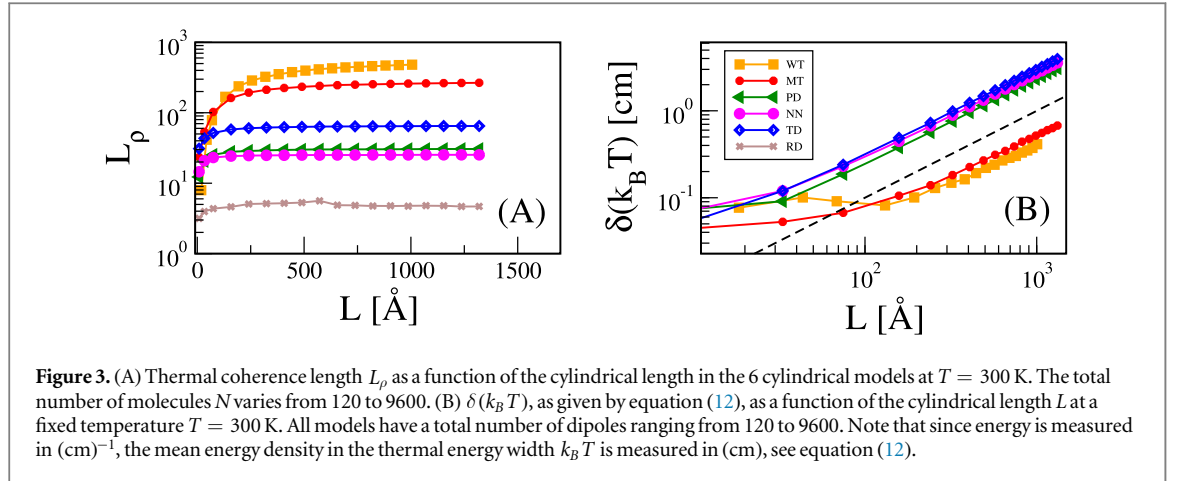
As a final remark for this section, let us note that for zero temperature L_ρ depends only on how much the ground state is delocalized, while for infinite temperature we have a fully mixed state with: $\hat{\rho} = (1/N)\sum_{i=1}^{N} |i\rangle \langle i|$, so that $L_\rho = 1$ as explained above even if all eigenstates are fully delocalized. On the other hand at finite temperature the thermal coherence length is determined by how much the energy eigenstates are delocalized on the site basis and also on how many eigenstates have an energy approximately within $k_B T$ above the ground state (i.e. from the density of states within an energy $k_B T$ from ground state). For this reason, it is important to study the delocalization properties of the eigenstates of the nanostructures considered here. This analysis is shown in appendix D, where we show that the eigenstates of all models but the RD one have fully delocalized eigenstates with a very similar degree of delocalization.

4.3. Analysis of the thermal coherence length

It is usually thought that natural photosynthetic structures can support delocalised states even at room temperature because the NN coupling between the molecules is larger than the room temperature energy $k_B T \approx 200$ cm^{-1}. In table 1 we show the NN coupling for the different models considered here. As one can see these couplings are larger than $k_B T$, and the maximal value between $\Omega_{1,2}$ are of the same order among the different models.

Let us now consider the thermal coherence length of the structures analysed here at room temperature. Figure 3(A) shows the dependence of L_ρ on the cylinder length L (with a corresponding number of dipoles N ranging from 120 to 9600).

In all models but the RD, the coherence length L_ρ increases quite markedly for small L until it reaches a plateau for larger L values. Apart from the RD structure, that exhibits a coherence length $L_\rho \approx 1$, the other structures are characterized by $1 \leqslant L_\rho \leqslant N$. This means that the thermal state at room temperature of these structures has a high degree of excitonic delocalization. Moreover it emerges clearly that the natural complexes (MT and WT) show the highest values of thermal coherence length if compared with the other mathematical structures. It is interesting to note that the MT complex supports a coherent delocalisation of the excitation over hundreds of molecules even at room temperature, which is one order of magnitude larger than the delocalisation supported by the NN model despite the fact that in the NN model the molecules have the same position and the same NN coupling of the MT model. This shows that the ability of such structures to support large delocalised excitation even at room temperature goes beyond the strength of the NN coupling between their molecules.

Figure 3. (A) Thermal coherence length L_ρ as a function of the cylindrical length in the 6 cylindrical models at $T = 300$ K. The total number of molecules N varies from 120 to 9600. (B) $\delta(k_B T)$, as given by equation (12), as a function of the cylindrical length L at a fixed temperature $T = 300$ K. All models have a total number of dipoles ranging from 120 to 9600. Note that since energy is measured in $(cm)^{-1}$, the mean energy density in the thermal energy width $k_B T$ is measured in (cm), see equation (12).

From figure 3(A) we can also deduce that the large coherence length of the natural systems cannot be explained by the presence of long range interactions. Indeed long-range interactions are present also in the PD and TD models, but their thermal coherence length is one order of magnitude smaller. By comparing the different cylindrical structures, one may also observe that the further the SRS is from the ground state, the lower is L_ρ. One could argue that natural structures concentrate the most radiative states (states with the largest dipole strength) close to the ground state in order to maximize their thermal coherence length. We will discuss the relationship between the presence of the SRS close to the ground state and a large coherence length in the next section.

The presence of a large thermal coherence length can be related to the structural properties of the energy spectrum. To this end we consider the mean density of states $\delta(k_B T)$ defined as the number of states contained in a unit of thermal energy $k_B T$ divided by $k_B T$, i.e.
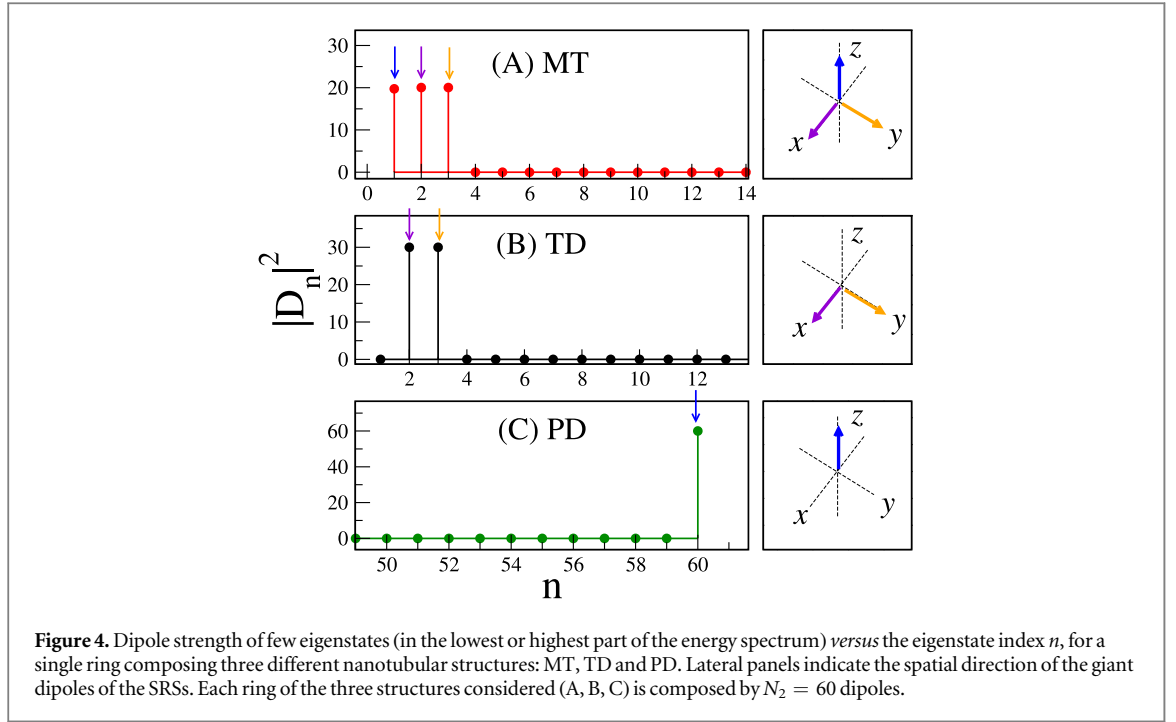
$$\delta(k_B T) = \frac{1}{k_B T} \int_{E_1}^{E_1 + k_B T} N(E) \, dE, \tag{12}$$

where E_1 is the ground state and $N(E)$ is the density of states (number of states per unit energy). In particular, we would like to study the dependence of the average density of states, equation (12) on the cylindrical length L. Results are shown in figure 3(B) and clearly indicate that not only, in general, the average density increases proportionally to L, but more importantly, natural structures are characterized by the smallest average densities (approximately one order of magnitude less than the other structures). Such a low density of states in the lower part of the spectrum induces, see figure 3(B), an enhanced thermal coherence length. Indeed, if all the eigenstates have approximately the same degree of delocalization, as measured by their PR for instance (see appendix D), then for a smaller number of states within an energy $k_B T$ from the ground state, the thermal coherence length is larger, as explained above. In order to explain the origin of the low density of states, let us observe that : (i) it cannot be due to the intensity of the NN coupling. Indeed the NN model, which has the same NN coupling as the MT model, has a much higher density of states and a smaller thermal coherence length; (ii) it cannot be due to the range of interaction since also the TD and PD model are characterized by the same interaction range but they display a higher density of states and as a consequence a smaller thermal coherence length. Below we propose an explanation of the connection between the presence of a SRS close to the ground state and a low density of states, implying a large thermal coherence length.

5. Relationship between structure and macroscopic coherence

In this section we propose an explanation of why such a low density of states is connected to the presence of SRSs close to the ground state of the system. As we will show below the low energy part of the spectrum for both the MT and WT models arises from a super-transfer coupling between states with a large (giant) dipole belonging to some sub-unit of the whole cylinder. In the case of MT we will show that the super-transfer coupling arises between giant dipole eigenstates of single rings, while in the case of WT the super-transfer arises between eigenstates belonging to different sub-units of the whole cylinder. The presence of super-transfer induces a large coupling energy which decreases the density of states. As a clear signature of this, we show below that super-transfer is also able to induce the emergence of an energy gap between the ground state and the first excited state.

Specifically in subsection 5.1 we analyse cylinders made of a sequence of rings and we show that the symmetry present in the system implies that each eigenstate of a ring couples only to a correspondent eigenstate of the other rings. We also show that the dipole strength of the eigenstates of each ring is concentrated in few SRSs. In subsection 5.2 we show that the coupling between SRSs in each ring displays a super-transfer effect,

Figure 4. Dipole strength of few eigenstates (in the lowest or highest part of the energy spectrum) *versus* the eigenstate index *n*, for a single ring composing three different nanotubular structures: MT, TD and PD. Lateral panels indicate the spatial direction of the giant dipoles of the SRSs. Each ring of the three structures considered (A, B, C) is composed by $N_2 = 60$ dipoles.

while the coupling between the subradiant states is characterized by a sub-transfer effect. Finally in subsection 5.3 we show how in natural structures the super-transfer coupling produces a depressed density of states close to the ground state, thus enhancing the thermal coherence length.

5.1. Structure of ring eigenstates coupling

In order to analyse the super-transfer effect, let us consider the properties of the eigenstates of the single rings composing three different nanotubes: MT, TD and PD. All the above mentioned models are composed of a sequence of rings, each containing 60 molecules, as explained in section 2. The case of the WT model will be discussed later since its structure is more complicated. In figure 4 the dipole strength of few eigenstates (ordered from low to high energy) of a single ring, containing 60 dipoles, is shown for the different structures. Note that the sum of all the dipole strengths must be equal to the number of the dipoles in the ring $N_2 = 60$ as explained in section 3. As one can see in the MT case the whole dipole strength is concentrated in the lowest three eigenstates, each having a dipole strength approximately equal to $N_2/3$. Each dipole strength is oriented in a different spatial position with the ground state having a dipole strength along *z* corresponding to the direction of the cylinder axis and the other two states perpendicular to it in the ring plane, see inset in figure 4(A). In the TD model in figure 4(B), the dipole strengths are concentrated in the first and second excited state (which are degenerate and having $|D_n|^2 = N_2/2$ each) and their direction lies in the plane perpendicular to the direction of the cylinder axis. Finally for the PD model in figure 4(C), the whole dipole strength is concentrated in the most excited state and it is directed along the *z*-axis (cylinder axis).

A common feature of these structures is their invariance under a $2\pi/N_2$ rotation around the cylinder axis. Strictly speaking, in the MT model such symmetry is slightly broken due to the presence of alternating α angles, see appendix A. Nevertheless since α is very small the change due to the symmetry breaking is negligible. As a consequence the Hamiltonian for each ring is a circulant matrix, i.e. each row can be obtained by a cyclic permutation of the previous one. Circulant matrices are diagonalized by the Fourier basis, so that the components of the eigenstates of each ring $|\varphi_q\rangle$ on the site basis $|j\rangle$ are given by
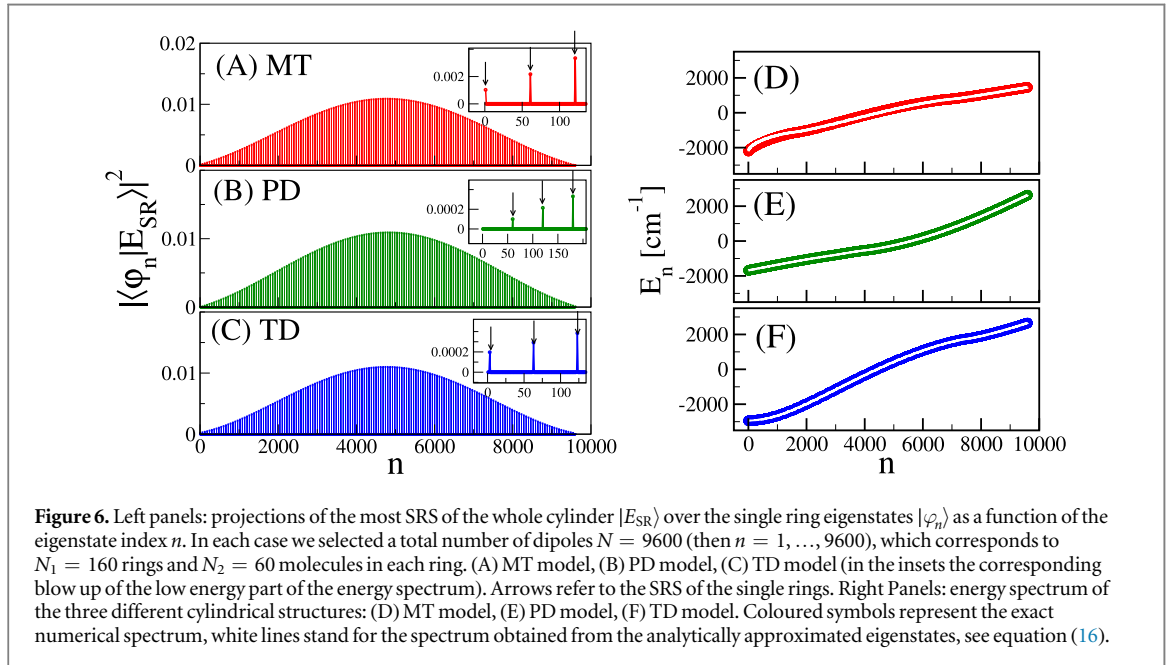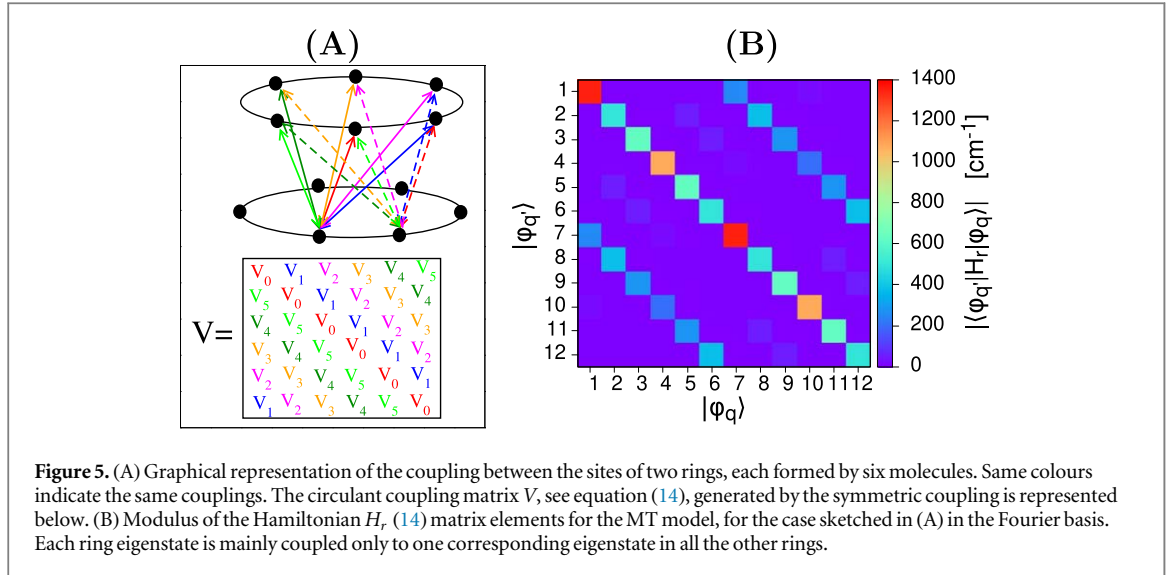
$$\langle j|\varphi_q\rangle = \frac{1}{\sqrt{N_2}}e^{i2\pi jq/N_2} \quad \text{for} \quad q = 1, \ldots, N_2. \tag{13}$$

Due to the rotational invariance the coupling matrix between two rings is also circulant.

To make explicit this point, let us work out a specific example of two rings. The Hamiltonian reads:

$$H_r = \begin{bmatrix} D & V \\ V & D \end{bmatrix}, \tag{14}$$

where *D* refers to the Hamiltonian of a single ring (which is diagonal in the Fourier basis given in equation (13)) and *V* represents the interaction between two rings. The total Hamiltonian matrix H_r can be made block diagonal by the matrix

Figure 5. (A) Graphical representation of the coupling between the sites of two rings, each formed by six molecules. Same colours indicate the same couplings. The circulant coupling matrix V, see equation (14), generated by the symmetric coupling is represented below. (B) Modulus of the Hamiltonian H_r (14) matrix elements for the MT model, for the case sketched in (A) in the Fourier basis. Each ring eigenstate is mainly coupled only to one corresponding eigenstate in all the other rings.

Figure 6. Left panels: projections of the most SRS of the whole cylinder $|E_{SR}\rangle$ over the single ring eigenstates $|\varphi_n\rangle$ as a function of the eigenstate index n. In each case we selected a total number of dipoles $N = 9600$ (then $n = 1, \ldots, 9600$), which corresponds to $N_1 = 160$ rings and $N_2 = 60$ molecules in each ring. (A) MT model, (B) PD model, (C) TD model (in the insets the corresponding blow up of the low energy part of the energy spectrum). Arrows refer to the SRS of the single rings. Right Panels: energy spectrum of the three different cylindrical structures: (D) MT model, (E) PD model, (F) TD model. Coloured symbols represent the exact numerical spectrum, white lines stand for the spectrum obtained from the analytically approximated eigenstates, see equation (16).

$$U_r = \begin{bmatrix} U & 0 \\ 0 & U \end{bmatrix},$$

where the elements of U are given by equation (13): $U_{j,q} = \langle j|\varphi_q\rangle$. In other words, each ring eigenstate is coupled only with one corresponding eigenstate of any other ring. This is clearly shown in figure 5(B), where the matrix elements of the Hamiltonian of a small cylinder composed of two rings of 6 sites each, are represented in the basis given by the tensor product of the Fourier basis of each ring. As one can see, this results in a block structure where each block has only diagonal elements.

As a consequence of the symmetric structure of the nanotubes considered above, all the eigenstates of the whole cylinder can be 'generated' by the coupling between the eigenstates of single rings, see also discussion in [69]. Specifically, the SRS of the whole cylinder is generated by the coupling of the SRSs of the single rings. In order to prove that, we show in figure 6(A)–(C) the most SRS for the different models projected along the eigenstates of the single rings. In the figure we considered cylinders made of $N_1 = 160$ rings, with $N_2 = 60$ molecules per ring, for a total number of dipoles of $N = 9600$. Let us analyse the single models individually.

(i) For the MT model, one can see that the most SRS (having a dipole along the cylinder axis) has components only on the ground states of the single rings (indicated by arrows in the inset of figure 6(A)) that are also SRSs with a dipole strength along the z-axis, see figure 4(A).

(ii) In the PD model, figure 6(B), the most SRS, $|E_{2814}\rangle$, projects itself on the most excited state in the single ring spectrum, which corresponds to the only SRS of the PD ring, see figure 4(C). Note that $|E_{2814}\rangle$ indicates the 2813rd excited state.

(iii) In the TD model there are two most SRSs which are degenerate with a different polarization: one along the x direction and one along the y direction. In figure 6(B) we considered only the SRS with a polarization along the y direction, which corresponds to the state $|E_{1083}\rangle$. Such state has non zero projections only onto the second excited states of the single ring with the same dipole direction of the SRS of the whole cylinder, see figure 4(B). Correspondingly the other SRS with a polarization along the x direction will have projection only on the SRS of the single ring with the same polarization.

These findings allow for a further approximate scheme for the eigenstates of the cylindrical structures considered above. Indeed, since each eigenstate of any single ring is coupled only to a corresponding eigenstate of the other rings, we can decompose the whole cylinder into independent chains where each site of the chain corresponds to a single ring eigenstate. For a chain having N_s sites and NN interactions the eigenstates are independent of the coupling and given by:

$$\langle k|\psi_r\rangle = \sqrt{\frac{2}{N_s + 1}} \sin\left(\frac{\pi k r}{N_s + 1}\right), \tag{15}$$

where k represents the site index and $r = 1, .., N_s$. Clearly when the interaction range is not NN, the above expression for the eigenstates is no longer valid. Nevertheless for the natural structures considered in this paper the interaction is short-range, decaying as $1/r^3$ for the realistic cylinder length considered here, so that in a first scheme we can consider the NN eigenstates as a good approximation. Note however that care should be taken to generalize such approximation since the interaction between the molecules is much more complicated than a simple dipole–dipole one. For instance the coupling is also affected by the dipole strength of the ring eigenstates involved as we will see below. Nevertheless we can assume that the chain of eigenstates is diagonalized by the same eigenstates of a chain with NN coupling for the parameters and the realistic system sizes considered here. Building the eigenstates as a tensor product between the Fourier basis for the ring (13) and the one for the chain (15)

$$\langle j, s \,|\Psi_{q,r}\rangle = \frac{1}{\sqrt{N_2}} e^{i 2\pi j q / N_2} \sqrt{\frac{2}{N_1 + 1}} \sin\left(\frac{\pi s r}{N_1 + 1}\right) \tag{16}$$

(with $j, q = 1, \ldots, N_2$ and $s, r = 1, \ldots, N_1$) we can diagonalize the Hamiltonian of the whole cylinder in order to obtain an approximation of the actual spectrum for the whole structures. The results are shown in figures 6(D)–(F) where the spectrum obtained from exact numerical diagonalization is compared with the spectrum obtained by diagonalizing the matrix with the eigenbase in equation (16). As one can see, the proposed analytic basis gives an excellent approximation of the spectrum obtained by exact numerical diagonalization.

5.2. Super and sub-transfer

In the previous section we have shown that each eigenstate of a single ring couples only with a corresponding eigenstate of the other rings (apart for a small symmetry breaking factor present in the MT model). Here we will show that the coupling between the eigenstates with a large dipole strength is enhanced with respect to the coupling between the single molecules within each ring by a factor proportional to the number of molecules placed on each ring. Such effect is known in literature as super-transfer [31]. At the same time we will show that the coupling between the eigenstates of the single rings with a small dipole strength is suppressed with respect to the coupling between the single molecules, giving rise to another collective sub-transfer effect, which has not been fully addressed in literature.
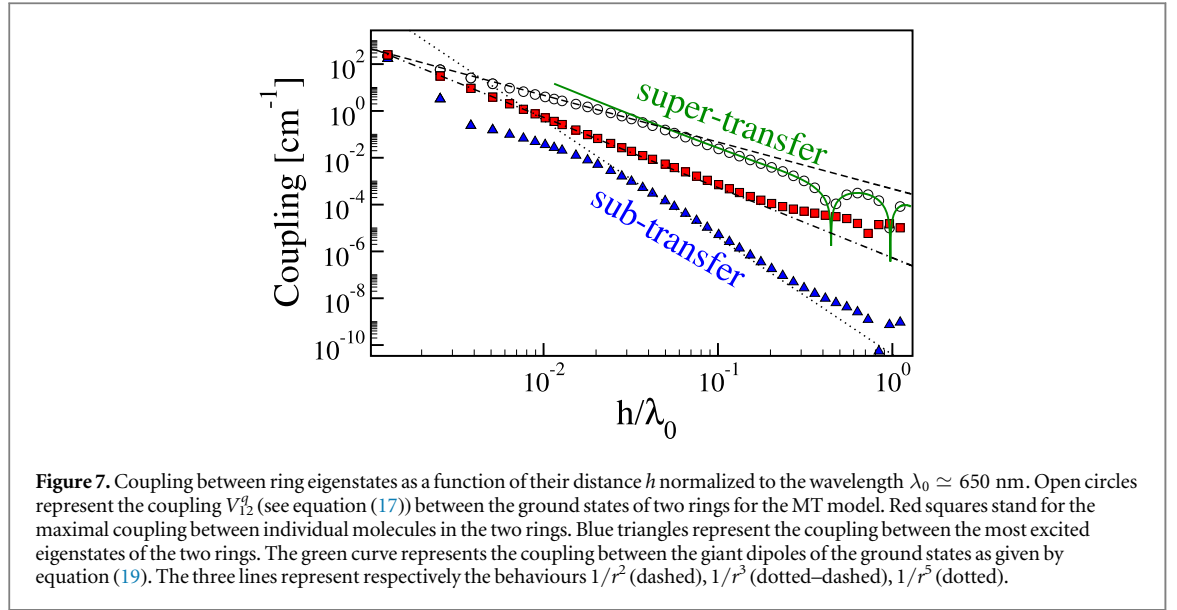
In order to prove the previous statements, let us compute the coupling strength between two eigenstates of two rings, say 1 and 2. Let us indicate the two corresponding qth eigenstates of the two rings as

$$|\psi^{s,q}\rangle = \sum_k C_k^{s,q} |k\rangle,$$

where the states $|k\rangle$ represent the site basis of a ring and $s = 1, 2$. The coupling between two single ring eigenstates belonging to two different rings can be written as:

$$V_{12}^q = \langle\psi^{1,q}|V|\psi^{2,q}\rangle = \sum_{k,k'} (C_k^{1,q})^* C_{k'}^{2,q} V_{k,k'}. \tag{17}$$

Using equations (3, 7) we have that $V_{k,k'} = \Delta_{k,k'} = f(r_{k,k'}) \vec{\mu}_k \cdot \vec{\mu}_{k'} + g(r_{k,k'})(\vec{\mu}_k \cdot \hat{r}_{k,k'})(\vec{\mu}_{k'} \cdot \hat{r}_{k,k'})$, where the functions f and g are implicitly defined by equation (3). When the distance between the two rings is much larger than their diameter we can approximate $r_{k,k'} \approx R_{12}$ where R_{12} is the distance between the centres of the two rings. In this limit, equation (17) becomes

Figure 7. Coupling between ring eigenstates as a function of their distance h normalized to the wavelength $\lambda_0 \simeq 650$ nm. Open circles represent the coupling V_{12}^q (see equation (17)) between the ground states of two rings for the MT model. Red squares stand for the maximal coupling between individual molecules in the two rings. Blue triangles represent the coupling between the most excited eigenstates of the two rings. The green curve represents the coupling between the giant dipoles of the ground states as given by equation (19). The three lines represent respectively the behaviours $1/r^2$ (dashed), $1/r^3$ (dotted–dashed), $1/r^5$ (dotted).

$$V_{12}^q = \sum_{k,k'} (C_k^{1,q})^* C_{k'}^{2,q} [f(R_{12}) \vec{\mu}_k \cdot \vec{\mu}_{k'} + g(R_{12})(\vec{\mu}_k \cdot \hat{R}_{12})(\vec{\mu}_{k'} \cdot \hat{R}_{12})], \tag{18}$$

which can be expressed in terms of the dipole strengths using equation (6)

$$V_{12}^q = [f(R_{12})|\vec{D}_q|^2 + g(R_{12})(\vec{D}_q \cdot \hat{R}_{12})(\vec{D}_q^* \cdot \hat{R}_{12})]. \tag{19}$$

As a result, we obtain $V_{12}^q \propto |D_q|^2 \propto N_2$. In other words the eigenstates with a large dipole strength will have a coupling enhanced by a factor proportional to the number of molecules N_2 in the ring.

The above expression represents the interaction between the giant dipoles of the eigenstates of each ring. Therefore states with a large dipole strength will have a super-transfer coupling, (proportional to the dipole strength of the eigenstates) increasing linearly with the number of molecules N_2 in each ring. At the same time, the coupling between two eigenstates with zero dipole strengths will be suppressed, leaving only higher order multipole terms to contribute to the coupling. This will lead to a sub-transfer coupling. The super and sub-transfer effects for the MT model are shown in figure 7 where we compare: (i) the coupling between the superradiant ground states (which have a large dipole strength) of two rings as a function of their rescaled distance (open circles); (ii) the maximal coupling between single molecules of each ring as a function of the distance between the two rings (red squares); (iii) the coupling between the most excited states (with a very small dipole strength) of each ring as a function of their distance (blue triangles).

Let us comment in detail this figure. First of all we note that the coupling between the states with a large dipole is clearly larger (by a factor $\sim N_2 = 60$) than the maximal coupling between the single molecules thus showing the super-transfer effect. Moreover, the coupling between the eigenstates with a small dipole strength is much smaller than the maximal coupling between single molecules: this shows the sub-transfer effect.

In the same figure, as a continuous green curve we show the coupling between the ground states as given by equation (19). As one can see, at sufficiently large distance, the couplings are well approximated by equation (19) thus confirming that the coupling is enhanced by a factor proportional to the number of molecules in each ring N_2.

Another important observation concerns the dependence of such couplings from the distance $r = h/\lambda_0$ and how it is modified by the super and sub-transfer effect. We can distinguish three different regimes: at small distances, at intermediate distances and at distances comparable with the wavelength of the optical transition. At large distances, when $h \sim \lambda_0$ an oscillatory behaviour arises due to the presence of oscillatory terms in the Hamiltonian of the system, see equation (7). At intermediate distances the super-transfer coupling decays with $1/r^3$ as the coupling between single molecules, consistently with the dipole–dipole nature of the interaction. On the other hand, the sub-transfer coupling decays as $1/r^5$ which is consistent with high order multipole expansion of the coupling since the dipole interaction is suppressed. At small distances the behaviour of the coupling with distance is less trivial: while the single molecule coupling still behaves as $1/r^3$, the sub-transfer coupling decays much faster and then it goes as $1/r^5$ as explained above. On the other hand the super-transfer coupling decays as $1/r^2$, which is much slower than the dipole coupling. Since all the couplings start from the same intensity at very small distances and the superradiant one has to go above the single molecule coupling, it makes sense that its decay is slower than $1/r^3$, but further analysis is needed to understand the origin of such slow decay of the interaction between giant dipoles.
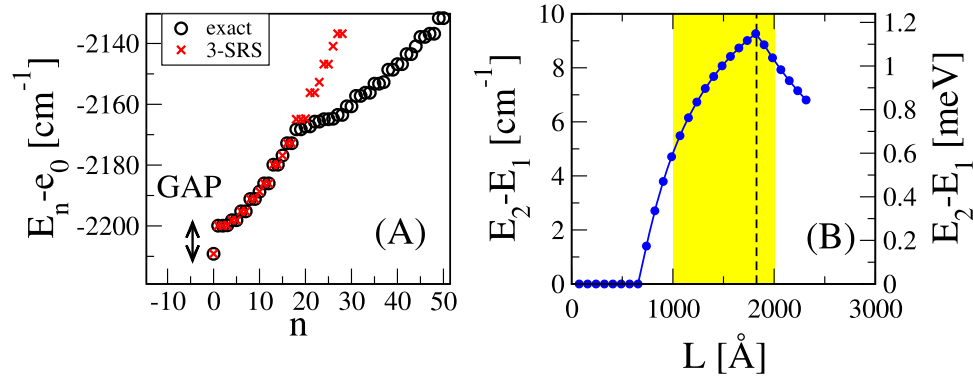
Figure 8. (A) The lowest part of the energy spectrum for a MT nanotube with 220 rings (open circles) compared with the spectrum generated by the super-transfer coupling between the the three most SRSs of each ring (crosses). Note the presence of a consistent energy gap between the ground state and the first excited state. (B) Energy gap (distance between the ground and the first excited state) for the MT model as a function of the nanotubular length. As one can see there is a region where the gap increases with the system size. Maximal gaps occurs at $L = 1826$ Å. The yellow vertical strip indicates the region where natural complexes operate.

5.3. Super-transfer and density of states

From the discussion above we can conclude that all the SRSs belonging to each ring will couple between themselves through a super-transfer coupling. For instance, in the case of the MT model, also the other two SRSs of the single rings corresponding to the first and second excited states will couple between themselves by super-transfer, see figure 4(A). While for the PD and the TD model the coupling between the SRS of the rings gives rise to the SRS of the whole cylinder, which lies far away from the ground state, for the MT model the coupling between the SRSs of the single rings determines completely the lowest part of the spectrum. In order to prove the last sentence we consider the $3N_1$ eigenvalues generated by the super-transfer coupling of the three SRSs for each ring of the MT model. The spectrum generated by the three SRSs is shown in figure 8(A) together with the exact spectrum of the MT model. As one can see this simple approximation allows to compute with high accuracy the lowest energy part of the spectrum. The presence of super-transfer induces a large coupling energy in the lowest part of the spectrum, which in turn diminishes the density of states. This is also signalled in figure 8(A) by the change of slope seen in the lower part of the spectrum. A further evidence of such decreased density of states induced by the super-transfer coupling of the SRS of each ring is shown in figure 8(B). Here the energy gap between the ground state and the first excited state for the MT model is shown as a function of the length of the nanotube. Contrary to what can be expected for generic systems, the energy gap increases with the system size instead of decreasing, up to a critical system size, above which it decreases. The maximal energy gap occurs at a distance of ∼182.6 nm which is compatible with the typical length of such nanostructures found in nature, ranging between 100 and 200 nm. Note that it would be interesting to understand the critical system size at which the gap has a maximum. We intend to study this problem in a future work.

The results obtained so far can be generalized to more complicated structures, such as the WT model, as the preliminary results shown in appendix E show. Indeed, even for the WT model, where the disposition of dipoles is much more complicated than in the previous models, one can show that the SRS close to the ground state emerges from the supertransfer coupling between the SRSs of cylindrical sub-units of the whole cylinder.

Summarizing, the analysis both for the MT and the WT models shows how a precise ordering of the dipoles in these systems can favour the emergence of super-transfer between the eigenstates of sub-units of the whole structure, producing an enhancement of the thermal coherence length. This represents a clear example of the interplay between structure and functionality. Moreover, let us notice that even if the other models (TD, PD) have a super-transfer coupling between the ring eigenstates with the largest dipole strength, the resulting SRS lies in the middle of the spectrum and its effect on the thermal coherence length is less relevant (since the latter is sensitive to the density of states only in the lowest part of the energy spectrum). This argument strongly supports the relationship between the presence of a SRS close to the ground state and the thermal coherence length discussed above. As a last remark, we would like to mention that in order to assess the ability of such structures to sustain a large macroscopic coherence length, also the effect of other sources of noise should be considered. A preliminary study of the effect of static energetic disorder on the thermal coherence length of the different models considered here is shown in appendix F. The results of our analysis clearly show that natural structures are able to protect macroscopic coherence up to values of the static disorder strength much larger than the typical disorder present in natural systems.
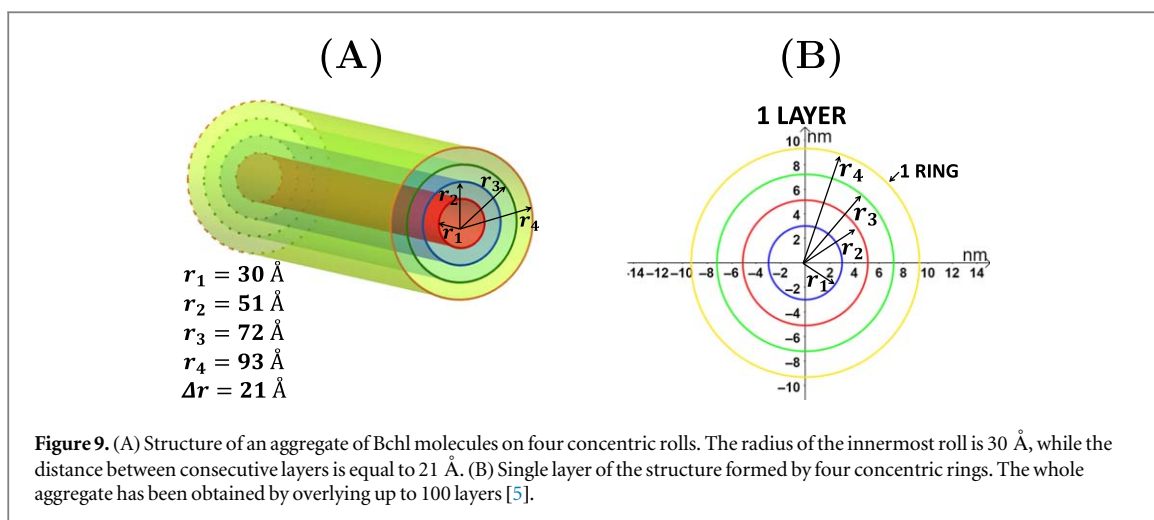
Figure 9. (A) Structure of an aggregate of Bchl molecules on four concentric rolls. The radius of the innermost roll is 30 Å, while the distance between consecutive layers is equal to 21 Å. (B) Single layer of the structure formed by four concentric rings. The whole aggregate has been obtained by overlying up to 100 layers [5].

Table 2. Main parameters used to engineer the structure with four concentric rolls.

Number of surfaces	4
Radius of the innermost roll	30 Å
Distance between concentric rolls	21 Å
Radii of the cylinders	$30 - 51 - 72 - 93$ Å
Number of dipoles on each ring	$30 - 51 - 72 - 93$
Density (number of dipoles over radius of the ring Å)	$1\,\text{Å}^{-1}$

6. Natural concentric structures

Natural antenna complexes in Green Sulphur Bacteria are not made by a single cylindrical surface. In order to take this into account, in this section we investigate a more complex configuration of dipoles on four concentric rolls as found in Green Sulphur bacteria *Chlorobium Tepidum*. Such structures have been extensively considered in literature (see for example [4, 54, 70, 71]). Inspired from these studies we considered here a model of *Chlorobium Tepidum* Triple mutant (bchQRU) formed by four concentric cylindrical surfaces, as shown in figure 9(A). Our aim is to investigate whether concentric cylindrical aggregates can support delocalized excitonic states at room temperature more efficiently than single cylindrical structures.

The distribution of the dipoles on each cylindrical surface is the same as the MT model of the previous section. In table 2 we report all parameters for this model.

The coupling between the EMF and the dipoles of the aggregate has been taken into account as in the Hamiltonian (7). As in the previous sections let us first analyse the dipole strengths associated with the eigenstates of the Hamiltonian (7).

Results are shown in figure 10(A) for a complex made of 80 layers of 4 concentric rings. As one can see the maximal dipole strength is concentrated in an energy region close to the ground state (the 43rd eigenstate has the maximal dipole strength, see inset in figure 10(A)).

Such dipole strength is associated with eigenstates having a high degree of delocalization along the cylinders. A further evidence is given in figure 10(B) where we show that the maximal dipole strength increases proportionally with the length *L* of the cylinders. We also note that the maximal dipole strength for concentric cylinders is between twice and 3 times larger than the maximal dipole strength of a single cylindrical surface with the same geometry, see figure 10(B) where the same data of figure 2(F) for the MT model have been reported for comparison. Note that the fact that concentric cylindrical surface can cooperate to create a larger SRS is not trivial since the interaction between molecules in different cylinders is very weak, equal to about $16\,\text{cm}^{-1}$ which is one or two orders of magnitude smaller than the coupling between molecules inside each cylinder, see table 1.

Finally, we have studied the effect of thermalization by putting the system in a thermal bath at room temperature $T = 300$ K. As before, we studied the thermal coherence length L_ρ, see equation (9).

Results are shown in figure 11(A) and compared with the same results obtained for the MT model. A fitting with the function
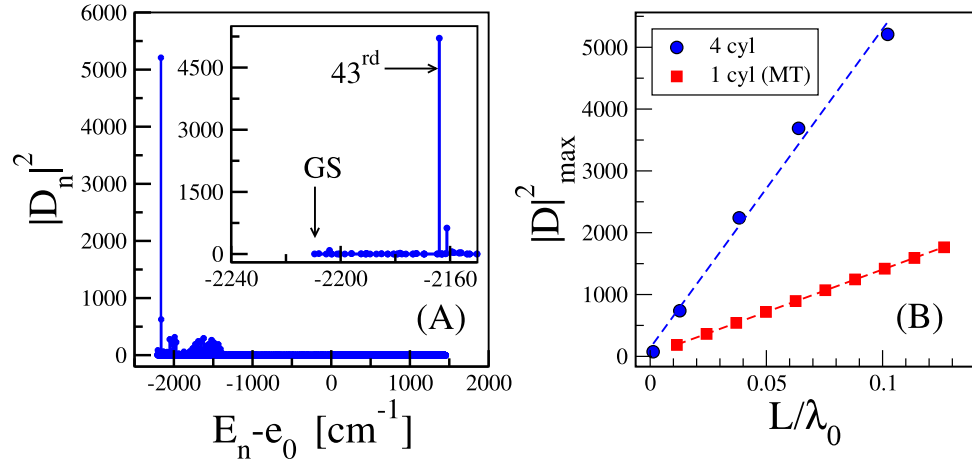
Figure 10. (A) Dipole strength associated with each eigenstates of the system composed of 80 layers of 4 concentric rings for a total length of $L = 65.57$ nm, as a function of the eigenvalues. Inset: the low energy part of the spectrum. Arrows indicate the ground state (GS) and the state with maximal dipole strength (the 43rd one). (B) Maximal dipole strength as a function of the rescaled length of the aggregate L/λ_0 where $\lambda_0 \approx 650$ nm. Dashed line represent the linear fits. Maximal length considered in this panel is $L = 65.57$ nm, corresponding to 80 layers of 4 concentric rings.
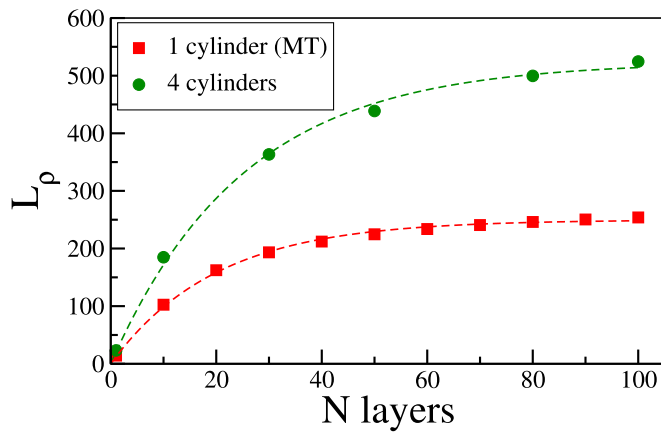
Figure 11. Thermal coherence length as a function of the number of layers in the cylinder for the system with four concentric cylinders (green circles) and the MT model with one cylinder only (red squares). Dashed lines are the fit with the expressions (20) whose parameters are $L_\infty = 249.8$ and $N_c = 19.9$ for the dashed green curve and $L_\infty = 523.9$ and $N_c = 25.2$ for the dashed red curve.

$$L_\rho = L_\infty(1 - e^{-N/N_c}), \tag{20}$$

shown in figure as dashed lines, gives for the asymptotic coherence length $L_\infty = 532.9$ for the 4 cylinders and $L_\infty = 249.8$ for the MT model. Keeping in mind that the radius of the cylinder for the MT model is an average of the four radii of the structure composed of 4 concentric cylinders, it is remarkable that the asymptotic coherence length is more than twice larger than the single cylindrical structure. This is highly non trivial, since for the concentric cylinders we have many more states and the density of states is larger than that for the single cylinder having the same length. For a discussion on this point see appendix G.

The results in this section show that packing symmetrical structures in concentric cylinders as it is found in natural photosynthetic complexes produces, at room temperature, a larger thermal coherence length than a single cylinder. In the future it would be important to study the robustness of the thermal coherence length of such aggregate of concentric cylinder to other sources of noise, such as static disorder, as it has been done for the single cylinders in appendix F. Even if the coupling between molecules belonging to different cylinders is quite weak, supertransfer coupling between sub-structures of the different cylinders might help to protect the coherence length of the whole aggregate to disorder. More analysis is needed to assess this point.

7. Conclusions and perspectives

We have analysed realistic structures of self-aggregated molecular nanotubes of chlorophyll molecules as found in Antenna Complexes of Green Sulphur Bacteria. By taking into account position and dipole orientation of chlorophyll molecules which agree with experimental data we have shown that natural structures are able to support macroscopic coherent states even at room temperature. Indeed in natural complexes we have found delocalized thermal excitonic states with a coherence length extending over hundreds of molecules. We show that such thermal coherence length is much larger than one could expect from the magnitude of the NN coupling and it cannot be explained even by the long-range nature of the interaction between the molecules. Instead, the ability of natural structures to support a large coherence length can be traced back to their specific geometric features.

In order to explain how this is possible, we first considered cylindrical structures made of a sequence of rings, each containing a fixed number of molecules equally spaced on the ring itself. Since the disposition of the dipoles is highly symmetric, in each ring we have few superradiant eigenstates (to which we associate a giant dipole) where most of the dipole strength of the system is concentrated, and many subradiant states with zero dipole strength. Moreover, due to the discrete rotational symmetry of the whole cylinder around its axis, each eigenstate of the ring sub-unit is coupled only with the correspondent eigenstate in the other rings. The coupling between the superradiant eigenstates in each ring gives rise to the super-transfer effect, i.e. a coupling which is enhanced by a factor proportional to the number of molecules in the ring. At the same time we have shown that the coupling between the subradiant states in each ring induces a sub-transfer effect, i.e. a suppressed coupling compared to the single molecule coupling. We have also demonstrated that in natural complexes the super-transfer coupling between the SRSs in each ring generates the lower part of the energy spectrum of the whole cylinder. Since the spectral energy width of a system is proportional to the intensity of the coupling between its parts, the enhanced super-transfer coupling is able to increase the spectral width close to the ground state. This creates a depressed density of states in the lower part of the spectrum, allowing for a larger thermal coherence length. Indeed the latter increases as the number of states in an interval $k_B T$ above the ground state decreases. We also gave evidence that similar mechanisms are responsible for the large thermal coherence length that we have found in other natural structures (WT model) where the disposition of the dipoles is less simple than the one described above.

From our results we can predict that symmetry in cylindrical molecular nanotubes is essential to have robust structures, not only to thermal noise, as we have demonstrated here, but also to other sources of noise such as static disorder, as our preliminary results have shown. The structural requirement is to create a super-transfer coupling between the superradiant eigenstates of cylindrical sub-units able to generate the lower part of the spectrum of the whole structure.

Molecular nanotubes are fundamental structures in biological systems and they are among the most promising structures to be used in quantum devices. The most important message which can be extracted from our analysis is the fact that specific geometric features, connected to symmetries, allow to control the cooperative effects in molecular aggregates. Indeed it is due to the presence of such cooperatively enhanced coupling (super-transfer) inside the molecular aggregates that macroscopic coherent states are allowed to survive at room temperature. This is an emergent property of such structures which cannot be reduced either to the intensity of the coupling between the molecules, or to their interaction range.

The relevance of geometry in molecular aggregates and the emergent properties arising from it are fundamental to understand even more complicated structures. For instance, structures made of few concentric cylinders as they are found in Green Sulphur bacteria. Our preliminary study of such structures has shown that these aggregates have an enhanced thermal coherence length compared to the single cylindric surfaces. We would like to mention that recently by some of the authors of this paper, excitonic states have been analysed also in microtubules [17], which are molecular nanotubes thought to be involved in many cellular functions. The analysis has confirmed the role of symmetry and geometry in such structures too. In the future it would be important to understand the general structural requirements necessary to induce macroscopic coherent states in generic molecular networks.

Finally, few clarifications are in order. Experimentally the presence of macroscopic coherence in molecular nanotubes can be verified by studying the absorption spectrum at room temperature. Also the role of super and sub-transfer can be detected experimentally analysing the dynamics of exciton transfer. Super and subtransfer could be detected either by controlling the initial state or by studying the long-time dynamics of the excitation transfer. In particular this study should reveal the presence of two different time scales (super and sub-transfer) in a similar way as the study of long-time excitation decay reveals super and sub-radiance, where sub-radiance implies a change of slope in the decay of the survival probability. For instance a time dependent diffusion coefficient might be an experimental signature of super and sub-transfer.

Even if we assumed thermal equilibrium in our structural analysis, it is possible that out-of-equilibrium processes can have an important role in molecular nanotubes. Indeed cooperative effects can induce time scales in a system which are faster or comparable with thermal relaxation time scales. We believe that the assumption of thermal equilibrium made in our analysis is adequate to assess the structural robustness of molecular nanotubes. Indeed

thermal equilibrium represents the worst case scenario for coherence and out-of-equilibrium processes should be characterized by even larger excitonic coherence lengths. For instance the initial state after the absorption of light is characterized by a very large coherence length due to the large wave-length ($\approx$700 nm) of the absorbed light with respect to the size of molecular nanotubes ($\approx$200 nm). After absorption the coherence length will decrease due to thermal relaxation, reaching its minimal value at thermal equilibrium. Thus processes which occurs out-of-equilibrium will be characterized by a larger coherence length.

The analysis presented in this manuscript is structural, and it has been made under the assumption of thermal equilibrium. The emergence of a macroscopic coherence length in molecular nanotubes even at room temperature is likely to have important consequences at the functional level. Indeed a large coherence length allows for excitonic giant dipoles to superabsorb light and to supertransfer excitations, thus enhancing the exciton diffusion coefficient. These effects have been studied in several realistic systems and are thought to play an important functional role in natural photosynthetic complexes. The results presented in this paper could explain the large efficiency of some natural photosynthetic complexes and they could inspire the engineering of efficient molecular aggregates for energy transport and light-harvesting. In perspective we plan to assess the functional role of macroscopic coherence in molecular aggregates both in equilibrium and out-of-equilibrium processes.

Acknowledgments

Appendix A. Geometry of the models

We analysed five different cylindrical models with fixed radius ($R = 60$ Å) and total number of molecules N, as shown in figure A1(A). These models differ for the geometrical arrangement of the chromophores (dipoles) along the cylindrical surface.

In order to describe how the dipoles are placed on the cylindrical surface let us unwrap it on a rectangular plane. In this plane the dipoles are disposed on the vertices of a lattice. The unit cell of the lattice in all structures is created starting from two lattice parameters a and b arranged in such a way that the angle between them is γ, see figure A1(B). Depending on the particular arrangement of the unit cell in the lattice the dipoles can be arranged into vertical chains or placed onto equal horizontal and coaxial rings. We assume that, in each of these structures, the shortest distance between two chromophores located on the same ring is $r_1 = 6.28$ Å. In our scheme all chromophores can be treated as dipoles with a constant squared dipole moment $|\mu|^2 = 30$ D^2 [61]. This corresponds to a dipole length $L_d = 1.14$ Å[7]. The ratio $L_d / r_1 \simeq 0.18$ is relatively small so that the dipole approximation can be successfully applied for the nearest-neighbour coupling.

In the following subsections we will analyse in detail the geometrical structures associated with each model.
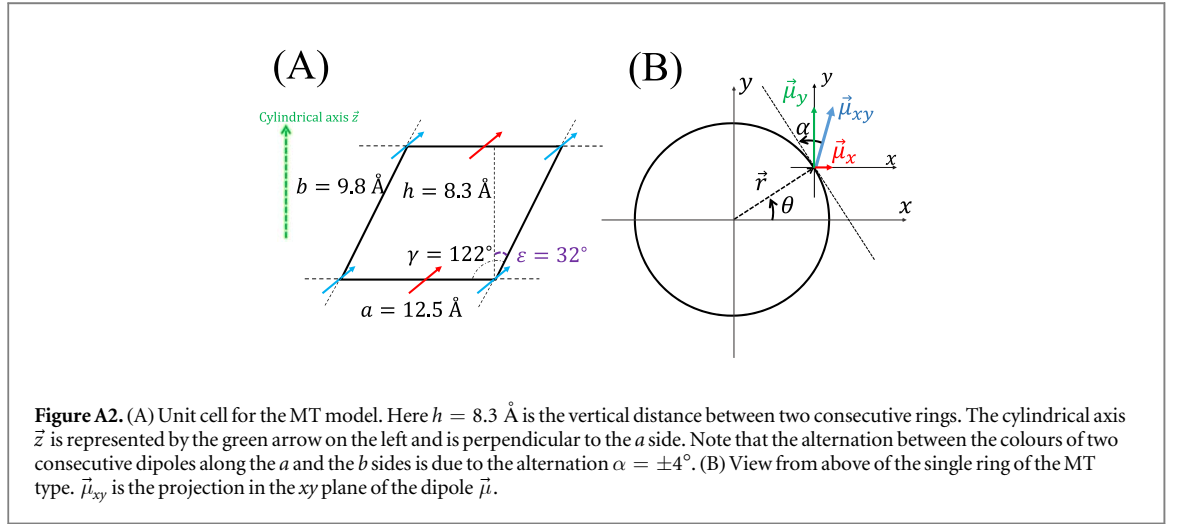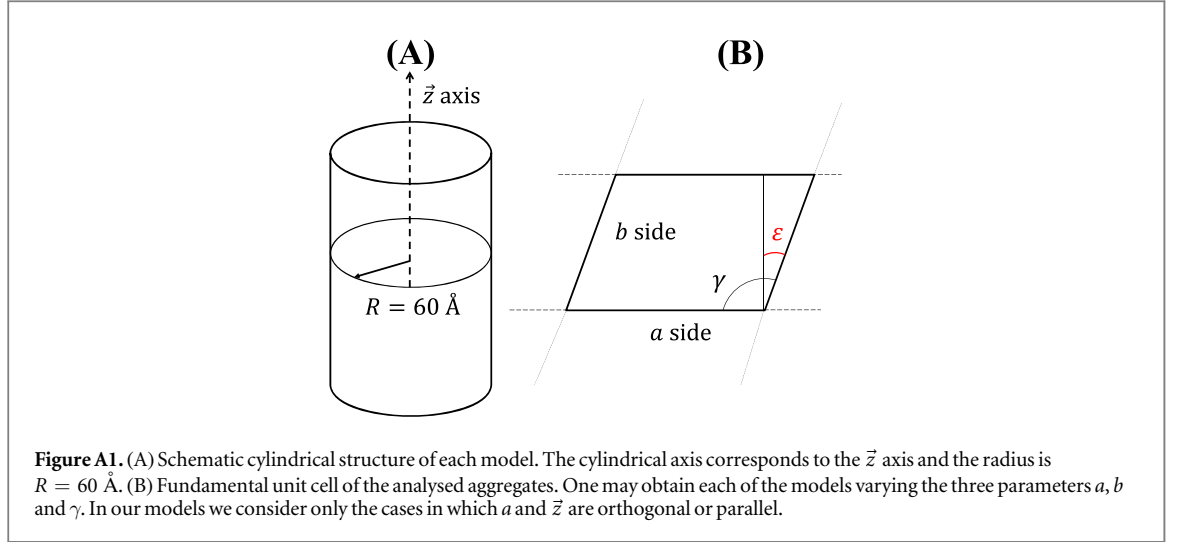
A.1. MT model
The MT model proposed here coincides with the Chlorobium Tepidum bchQRU triple mutant investigated in other studies ([53, 54, 56]).

In the MT cylindrical structure, the total number N of chromophores is organized into N_1 equal, horizontal and coaxial rings, see figure 1(A) in the main text. Each ring contains $N_2 = 60$ chromophores and two consecutive rings are separated by a vertical distance $h = 8.3$ Å. In the unit cell, shown in figure A2(A), h is parallel while a is perpendicular to the cylindrical axis $\vec{z}$. Any chromophore along the surface will be labelled as the n_2th dipole on the n_1th ring (where $n_1 = 1, ..., N_1$ and $n_2 = 1, ..., N_2$). Since we keep the radius R fixed, the density of chromophores along each ring is also fixed: $\rho_s = (2\pi$ Å$)^{-1}$. The position of each dipole onto the cylindrical surface is characterized by two cylindrical coordinates. Nevertheless it is useful to introduce three angles (the latter being dependent on the first and second):

- $\varphi = 360°/N_2 = 6°$ is the azimuthal angle between two adjacent dipoles in the same ring,

- $\xi = h \tan \varepsilon /R \simeq 4.956°$ is the twist angle between two successive dipoles located onto neighbour rings,

---

[7] In terms of ESU-CGS and Gaussian units one may observe that $1D = 10^{-6}$ cm g$^{1/2}$ s^{-1} Å$^{3/2}$ and the elementary charge is $|e^-| = 4.803\,204\,25 \times 10^{-10}$ cm$^{3/2}$ g$^{1/2}$ s^{-1}. From the relation $L_d = \mu/e^-$ we obtain $L_d = 1.14$ Å.

Figure A1. (A) Schematic cylindrical structure of each model. The cylindrical axis corresponds to the $\vec{z}$ axis and the radius is $R = 60$ Å. (B) Fundamental unit cell of the analysed aggregates. One may obtain each of the models varying the three parameters a, b and γ. In our models we consider only the cases in which a and $\vec{z}$ are orthogonal or parallel.

Figure A2. (A) Unit cell for the MT model. Here $h = 8.3$ Å is the vertical distance between two consecutive rings. The cylindrical axis $\vec{z}$ is represented by the green arrow on the left and is perpendicular to the a side. Note that the alternation between the colours of two consecutive dipoles along the a and the b sides is due to the alternation $\alpha = \pm 4°$. (B) View from above of the single ring of the MT type. $\vec{\mu}_{xy}$ is the projection in the xy plane of the dipole $\vec{\mu}$.

- $\theta = n_1 \xi + n_2 \varphi$ is the angle between the position $\vec{r}$ of the dipole and the x axis.

In this way we have :

$$r_x = R \cos\theta$$
$$r_y = R \sin\theta$$
$$r_z = h(n_1 - 1). \tag{A.1}$$

The components of the dipole moment $\vec{\mu}$ can be expressed through two angles:

- $\alpha = 4°$, between the projection of the dipole moment onto the plane of the ring and the plane tangent to the cylindrical surface, see figure A2(B).

- $\beta = 55°$, is the angle created by the single dipole moment with the cylindrical axis.

Assuming the n_2th dipole with an angle $\alpha = +4°$, the $(n_2 + 1)$th dipole will have $\alpha = -4°$, the $(n_2 + 2)$th dipole $\alpha = +4°$ and so on. This alternation is valid along the a direction and makes consecutive dipoles to point inward ($\alpha = +4°$) and outward ($\alpha = -4°$) respectively. Generally, we have that the generic dipole moment $\vec{\mu}$ has the following normalized components expressed in terms of spherical coordinates:

$$\mu_x = -\sin\beta \sin(\theta + (-1)^{n_2} \cdot \alpha)$$
$$\mu_y = \sin\beta \cos(\theta + (-1)^{n_2} \cdot \alpha)$$
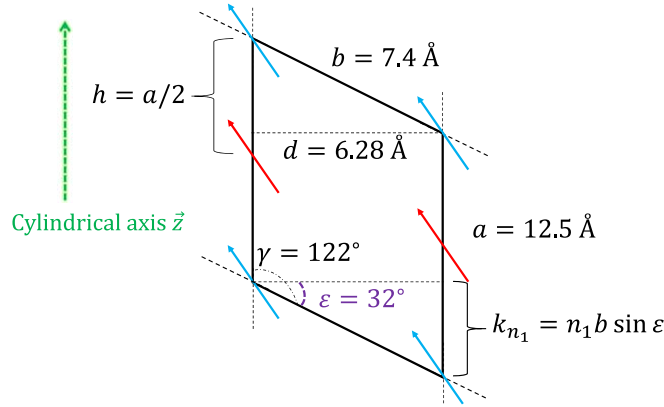$$\mu_z = \cos\beta. \tag{A.2}$$

Figure A3. Unit cell for the WT model. Here k_{n_1} refers to the vertical shift of two dipoles belonging to two nearest-neighbour chains, while d is the distance between two chains. Two consecutive dipoles on the same chain are separated just by a quantity equal to $a/2$. One can notice that this unit cell is the rotation by $90°$ around $\vec{z}$ of the previous unit cell for the MT model (figure A2), but with different parameters. The alternation of two colours of two consecutive dipoles along the a and the b direction represents the typical alternation $\alpha = \pm 4°$.
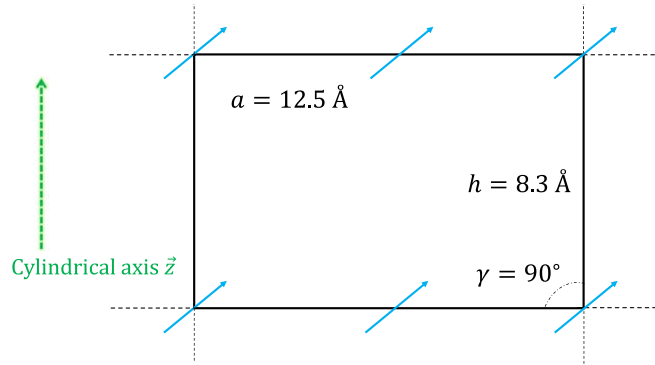

Figure A4. Unit cell for the PD, TD and RD models. Here the parameter b coincides with the vertical distance h between two consecutive rings. The cylindrical structure is obtained wrapping this rectangular unit cell around the direction of $\vec{z}$, which is perpendicular to the a side.

A.2. WT model

The WT model [53, 54, 56] shows a deep structural difference compared to the other structures. Indeed it can be thought as organized into N_1 vertical chains and each of them with N_2 molecules. So one can talk about the n_2th chromophore on the n_1th chain with $n_1 = 1, \ldots, N_1$ and $n_2 = 1, \ldots, N_2$. Dipoles moments on adjacent chains do not have the same height but they are shifted by a quantity $k_{n_1} = n_1 b \sin \varepsilon$ to originate a helical structure, as shown in figure 1(B) of the main text. The lattice has the following parameters: $a = 12.5$ Å, $b = 7.4$ Å, $\gamma = 122°$ and $\varepsilon = 32°$. The unit cell of the WT type is similar to that of the MT, but it is rotated by an angle $90°$ around the $\vec{z}$ direction, see figure A3, so the vertical distance between two dipoles on the same chain measures $h = a/2 = 6.25$ Å. Moreover $\varphi = 360°/N_1 = 6°$ will be intended as the azimuthal angle between adjacent chains, and $\theta = n_2 \varphi$ as the angle between the position vector $\vec{r}$ and the x axis. The position of the generic dipole on the surface can be expressed in cylindrical coordinates as follows:

$$
\begin{aligned}
r_x &= R \cos \theta \\
r_y &= R \sin \theta \\
r_z &= h(n_2 - 1) + k_{n_1}.
\end{aligned}
\tag{A.3}
$$

The components of each dipole moment are given by equation (A.2) with $\alpha = 4°$, $\beta = 35°$. Also in the WT model there is the alternation $\alpha = +4°$ and $\alpha = -4°$ between consecutive dipoles.
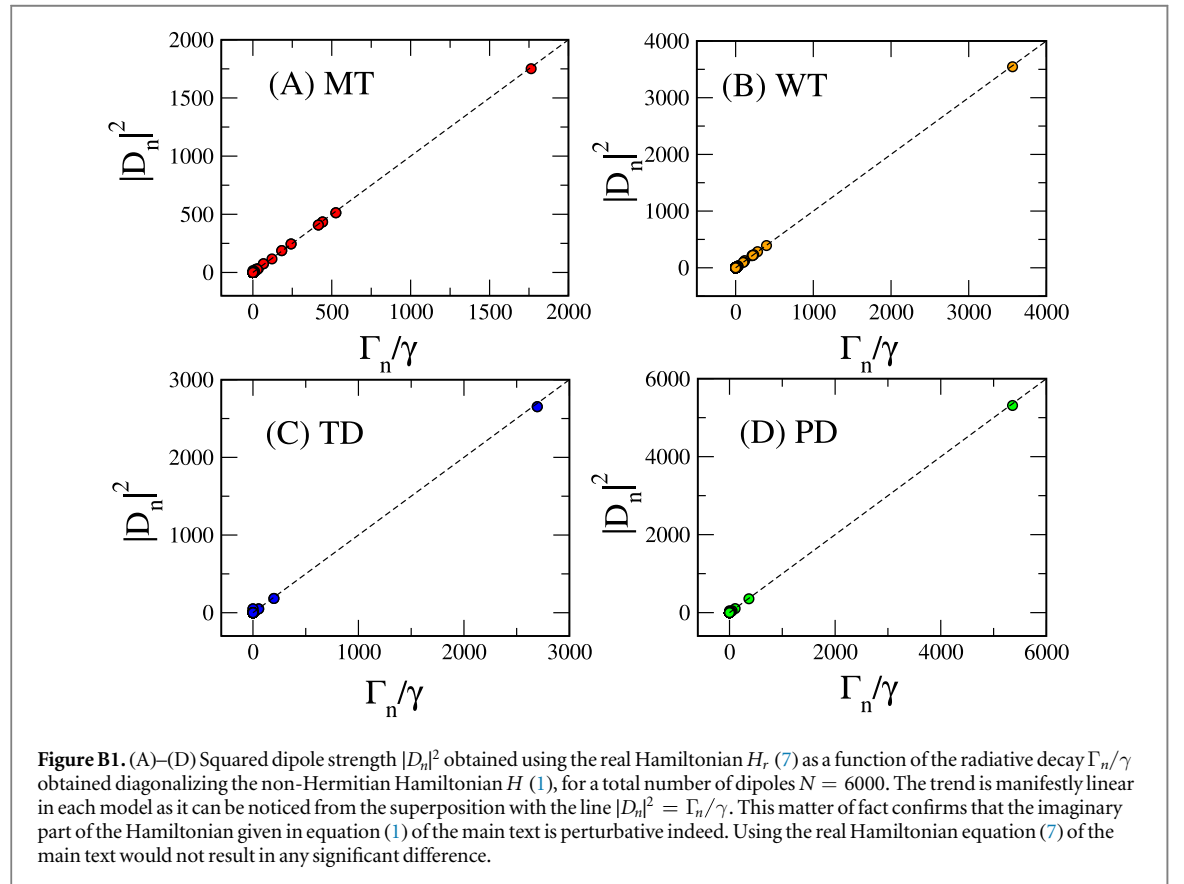
A.3. PD, TD and RD models

These models, shown in figures 1(C)–(E) of the main text do not exist in nature and they have been introduced only for comparison with the natural systems. They exhibit a different lattice compared to the natural

complexes, since the unit cell is a rectangle. As shown in figure A4 we have $\gamma = 90°$, $a = 12.5$ Å and $b = h = 8.3$ Å. The cylindrical axis $\vec{z}$ is perpendicular to the a side and one could build each of the three structures wrapping up the lattice around it. The three cylinders have again the same radius $R = 60$ Å and the same number of molecules N. Also, they are arranged into N_1 equal, horizontal and coaxial rings such that each of them carries N_2 dipoles. Once again a particular dipole moment will be indicated as the n_2 th chromophore on the n_1 th ring ($n_1 = 1, …, N_1$ and $n_2 = 1, …, N_2$). The three models differ for the values of α, β in the following way:

- in the PD structure, $\beta = 0°$ and $\alpha = 0°$,

- in the TD structure, $\beta = 90°$ and $\alpha = 0°$,

- in the RD structure, the angles are uniformly distributed such that $\alpha \in [0, 360°]$ and $\beta \in [0, 180°]$.
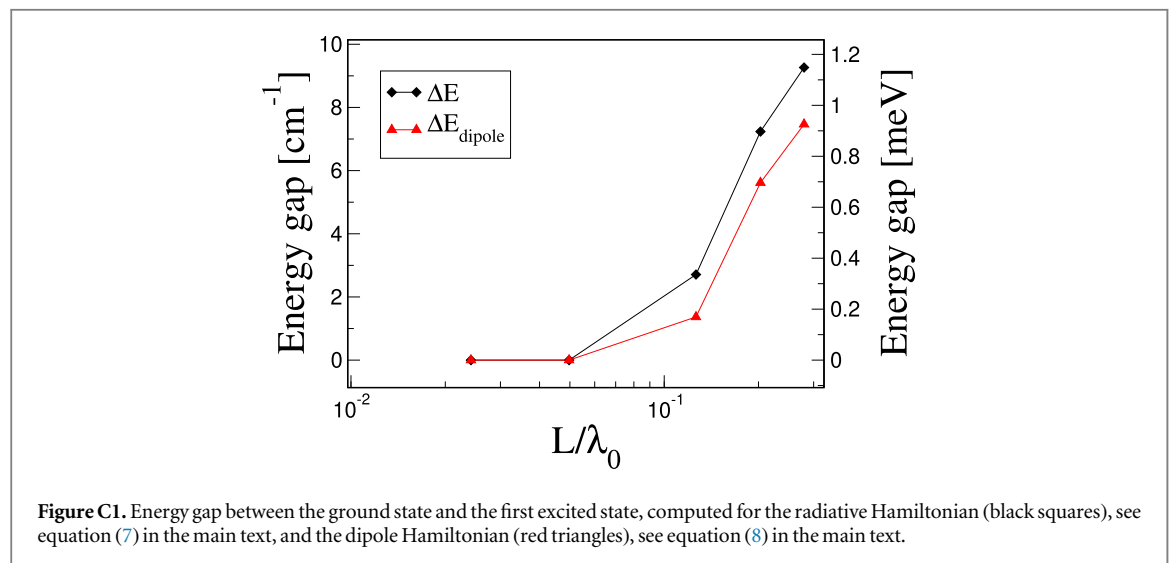
Appendix B. Comparison between dipole strengths and radiative decay widths

In figure B1 the comparison between the dipole strengths $|D_n|^2$ (obtained using the Hamiltonian H_r (7)) and the rescaled radiative widths Γ_n/γ (obtained diagonalizing the Non-Hermitian Hamiltonian H (1)) is shown for all the eigenstates of the MT, WT, TD and PD models for $N = 6000$ dipoles. As one can see the two quantities can be considered to be the same (compare symbols with the dashed lines, which represent the behaviours $|D_n|^2 = \Gamma_n/\gamma$).

Figure B1. (A)–(D) Squared dipole strength $|D_n|^2$ obtained using the real Hamiltonian H_r (7) as a function of the radiative decay Γ_n/γ obtained diagonalizing the non-Hermitian Hamiltonian H (1), for a total number of dipoles $N = 6000$. The trend is manifestly linear in each model as it can be noticed from the superposition with the line $|D_n|^2 = \Gamma_n/\gamma$. This matter of fact confirms that the imaginary part of the Hamiltonian given in equation (1) of the main text is perturbative indeed. Using the real Hamiltonian equation (7) of the main text would not result in any significant difference.

Appendix C. Comparison between radiative and dipole approximations

In order to understand the validity of the dipole approximation in the range of sizes of the natural systems considered, we have compared the dipole Hamiltonian, see equation (8) in the main text, with the radiative Hamiltonian, see equation (7) in the main text, which we used in our paper. For instance comparing the dipole strength and the energy of the SRS we have found that the dipole approximation is good for both quantities, with a relative error which increases with the system size, but it remains small up to the value of $L/\lambda_0 \approx 0.3$ where the relative error of the dipole strength is 0.1% and the relative error of the energies is 0.02%. Nevertheless in other quantities, such as the energy gap between the ground state and the first excited state, the error can be as large as 20%, see figure C1. Thus, we can say that while the dipole approximation seems to be well justified for the typical sizes of natural nanotubes, nevertheless non-negligible deviations can be found in some relevant quantities. For this reason here we used the radiative Hamiltonian which is more accurate. Moreover, one should not forget that the errors increase with the system size.

Figure C1. Energy gap between the ground state and the first excited state, computed for the radiative Hamiltonian (black squares), see equation (7) in the main text, and the dipole Hamiltonian (red triangles), see equation (8) in the main text.
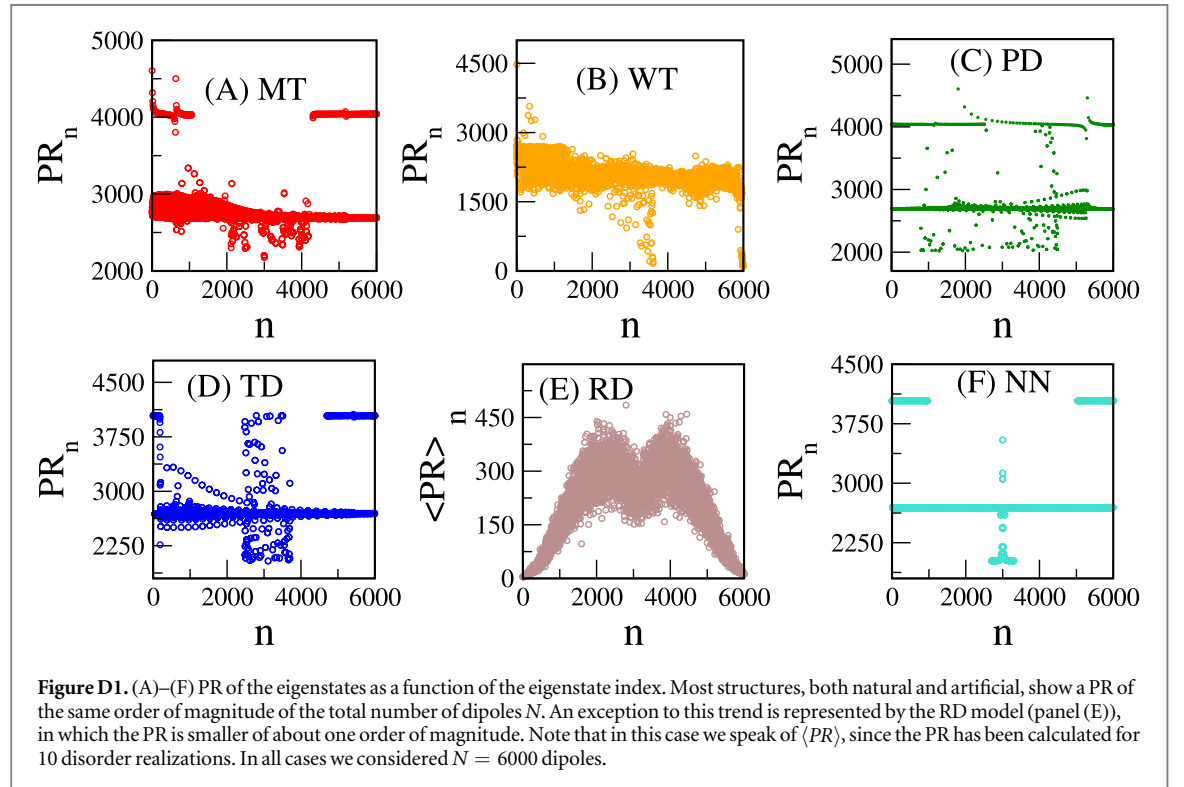
Appendix D. Participation ratio (PR) of the eigenstates

As a measure of delocalization of the eigenstates of the different nanotubular structures, we analyse the PR of the eigenstates. Let us take into account the expression (5) of the *n*th energy eigenstate on the site basis: the coefficient C_{ni} indicates its component on the *i*th site. The PR of the *n*th eigenstate is defined as follows:

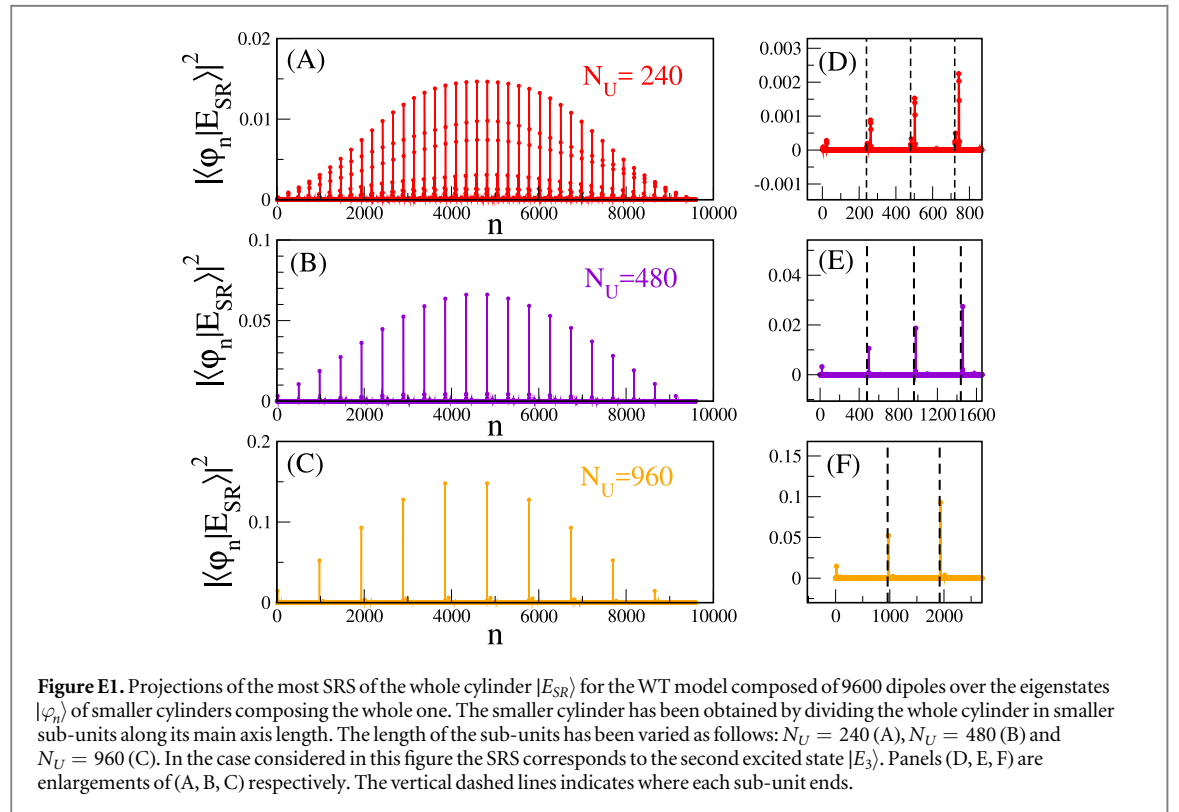$$PR_n = \frac{1}{\sum_{i=1}^{N}|C_{ni}|^4}. \tag{D.1}$$

Generally speaking, $PR_n \sim o(N)$ stands for a suitable degree of delocalization of the *n*th eigenstate, while we have $PR = 1$ for a state fully localized on a single site. Figure D1 shows how the PR of each eigenstate depends on the eigenstate index in the six cylindrical models examined so far. All models but the RD (E) exhibit a PR of the same order, such that $PR_n \sim o(N)$. One may observe indeed a difference of about one order of magnitude between the RD aggregate and the other structures. The presence of low degree of delocalization in the RD model is expected since the random coupling matrix elements between molecules can induce Anderson localization [72].

Note that the expression of L_ρ in equation (9) is not equivalent to the PR even for the case of a density matrix describing a pure state. Nevertheless both L_ρ and the PR are a measure of delocalization.

Figure D1. (A)–(F) PR of the eigenstates as a function of the eigenstate index. Most structures, both natural and artificial, show a PR of the same order of magnitude of the total number of dipoles *N*. An exception to this trend is represented by the RD model (panel (E)), in which the PR is smaller of about one order of magnitude. Note that in this case we speak of $\langle PR \rangle$, since the PR has been calculated for 10 disorder realizations. In all cases we considered $N = 6000$ dipoles.

Appendix E. Super-transfer in the WT model

The WT model is more complicated than the other models since the dipoles are not arranged into rings, but rather into helical structures. Nevertheless a very highly symmetrical disposition of the dipoles is also present in this case and one can think that the super-transfer coupling between the eigenstates of sub-units of the whole cylinder might influence the lowest part of the spectrum even for this model. In order to show this fact, we have split the whole cylinder along the axis direction (the *z* direction) into smaller cylindrical structures. Each smaller cylinder contains a variable number of dipoles N_U. The projection of the SRS of a cylinder of 9600 dipoles on the eigenstates of these sub-units is shown in figure E1 for different values $N_U = 240, 480, 960$. For a WT cylinder of 9600 dipoles the SRS lies in the lowest part of the spectrum and it corresponds to the second excited state with a dipole strength directed along the *z*-axis. As one can see from figure E1 the SRS of the whole cylinder has components mainly on one eigenstate for each sub-unit. We checked that such eigenstate corresponds to a SRS of each sub-unit with a dipole strength directed along the *z*-axis. Since the SRSs of each sub-unit have a giant dipole strength they couple by super-transfer. This shows that also for the WT model the super-transfer coupling inside the cylindrical structure might be responsible for the low density of states close to the ground state energy, see figure 3(B). Nevertheless further analysis is needed to confirm this conjecture for the WT model. Let us note that the fact that the decomposition in sub-units of different sizes shows a similar pattern is a signature of the self similar behaviour present in such structures, which has been observed also in other molecular nanotubes [17]. Clearly if one chooses too small subunits the self-similar behaviour disappears. For instance in our case if we take a block of 60 molecules the SRS of the whole structure is not concentrated mostly on one eigenstate of the block.

Figure E1. Projections of the most SRS of the whole cylinder $|E_{SR}\rangle$ for the WT model composed of 9600 dipoles over the eigenstates $|\varphi_n\rangle$ of smaller cylinders composing the whole one. The smaller cylinder has been obtained by dividing the whole cylinder in smaller sub-units along its main axis length. The length of the sub-units has been varied as follows: $N_U = 240$ (A), $N_U = 480$ (B) and $N_U = 960$ (C). In the case considered in this figure the SRS corresponds to the second excited state $|E_3\rangle$. Panels (D, E, F) are enlargements of (A, B, C) respectively. The vertical dashed lines indicates where each sub-unit ends.

Appendix F. Robustness to static disorder

In order to study the robustness of the thermal coherence length as defined in equations (9) and (11) to other sources of noise, here we consider the effect of static disorder i.e. time-independent and space-dependent fluctuations of the excitation energies of the molecules comprising the molecular nanotube. Specifically, we consider that the excitation energies are uniformly distributed around the initial value e_0, between $e_0 - W/2$ and $e_0 + W/2$, so that W represents the strength of the static disorder. It is well known that static disorder induces localization of the system eigenstates, a phenomenon known as Anderson localization [72]. Due to this effect, for large disorder, the probability to find the excitation is concentrated on very few sites, eventually on one site only, for extremely large disorder. Anderson localization usually occurs in presence of short-range interactions, which is not our case, since interaction results from a complicated power law, see equation (1). Therefore the results of our analysis are in principle not obvious. In figure F1 the thermal coherence length for $T = 300$ K is shown as a function of the static disorder strength, normalized to $k_B T$ with $T = 300$ K. As one can see the natural models (MT and WT) retain their larger thermal coherence length even in presence of static disorder up to $W \approx 10 k_B T$. This energy scale is much larger than the static disorder expected in natural systems which is of the order of $k_B T$. Thus, our preliminary results, even if cylinders with only 6000 dipoles have been considered, show that such structures are able to sustain a large thermal coherence length even in presence of static disorder.
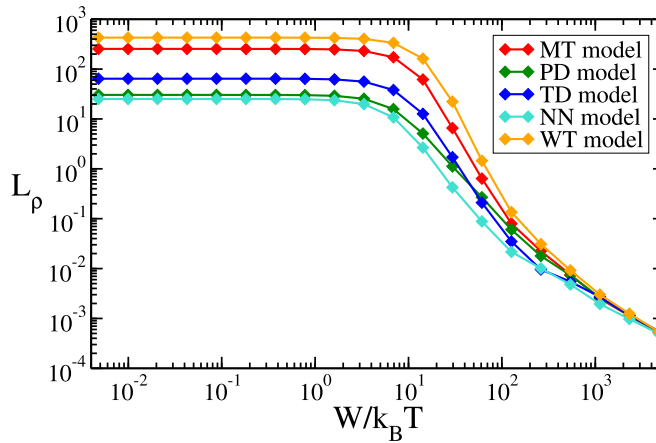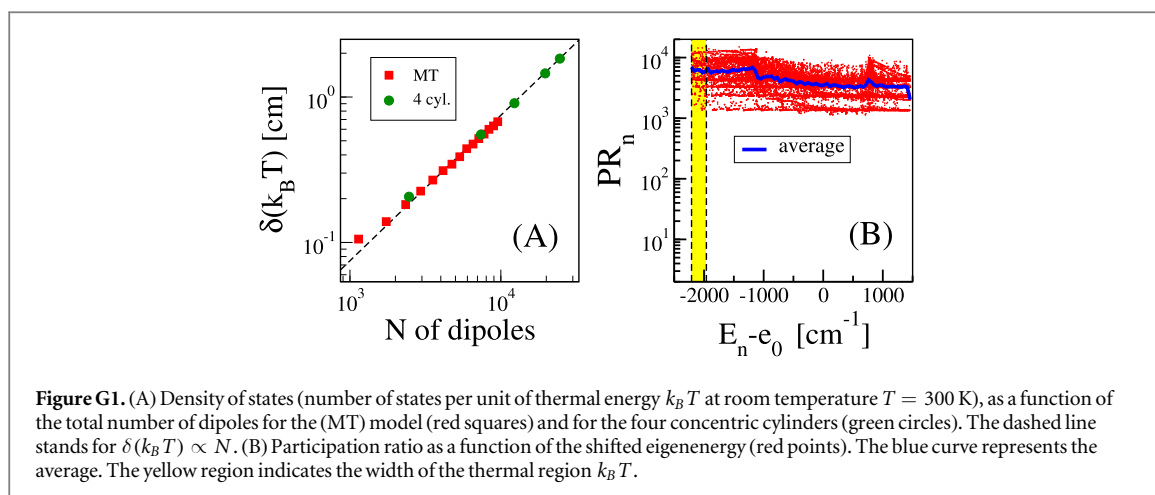

Figure F1. Thermal coherence length versus the normalized strength of static disorder $W/k_B T$, with $T = 300$ K for different models as indicated in the legend. In all models we considered $N = 6000$ dipoles. An average of over 20 realizations of disorder has been done for each disordered strength.

Figure G1. (A) Density of states (number of states per unit of thermal energy $k_B T$ at room temperature $T = 300$ K), as a function of the total number of dipoles for the (MT) model (red squares) and for the four concentric cylinders (green circles). The dashed line stands for $\delta(k_B T) \propto N$. (B) Participation ratio as a function of the shifted eigenenergy (red points). The blue curve represents the average. The yellow region indicates the width of the thermal region $k_B T$.

Appendix G. Concentric cylinders

Let us emphasize that the fact that the thermal coherence length for the four concentric cylinders is larger than the thermal coherence length of the single cylinder. This is highly non trivial. Indeed, in the case of four concentric cylinders we have many more states and the density of states is larger than that of a single cylinder having the same length. In order to explain better this point, let us compute the density of states $\delta(k_B T)$ in a unit of thermal energy $k_B T$ for different numbers of dipoles N, see equation (12) in the main text. This is shown in figure G1 for both the concentric cylinders model and the MT, see figure G1(A). As one can see the density of states is exactly the same for the two models as a function of the number of dipoles N. Nevertheless for the same fixed length, the density of states for the four concentric cylinders is larger than the density of the single cylinder. Despite this, a large thermal delocalisation length for the concentric cylinder case can be explained by the fact that the eigenstates for the 4 concentric cylinders are delocalised over a larger number of molecules as it is shown in figure G1(B).

ORCID iDs

Francesco Mattiotti ⓘ https://orcid.org/0000-0002-2532-8876
Fausto Borgonovi ⓘ https://orcid.org/0000-0002-9730-1189
Giuseppe Luca Celardo ⓘ https://orcid.org/0000-0002-3679-1954

References

[1] Engel G S *et al* 2007 *Nature* **446** 782
[2] Panitchayangkoon G *et al* 2010 *Proc. Natl Acad. Sci. USA* **107** 12766
[3] Scholes G D *et al* 2017 *Nature* **543** 647
[4] Huh J, Saikin S K, Brookes J C, Valleau S, Fujita T and Aspuru-Guzik A 2014 *J. Am. Chem. Soc.* **136** 2048
[5] Sawaya N P D, Huh J, Saikin S K, Fujita T, Saikin S K and Aspuru-Guzik A 2015 *Nano Lett.* **136** 1722
[6] Fetisova Z, Freiberg A and Timpmann K 1988 *Nature* **334** 633
[7] Fetisova Z, Freiberg A, Mauring K, Novoderezhkin V, Taisova A and Timpmann K 1996 *Biophys. J.* **71** 995
[8] Fetisova Z, Freiberg A, Mauring K, Novoderezhkin V, Taisova A and Timpmann K 1996 *FEBS Lett.* **383** 233
[9] Knoester J 2006 *Int. J. Photoenergy* **2006** 61364
[10] Didraga C and Knoester J 2004 *J. Lumin.* **110** 239
[11] Molina R A, Benito-Matías E, Somoza A D, Chen L and Zhao Y 2016 *Phys. Rev.* E **93** 022414
[12] Chenu A, Keren N, Paltiel Y, Nevo R and Cao J 2017 *Phys. Chem.* B **121** 9196
[13] Eisenberg I *et al* 2014 *Phys. Chem. Chem. Phys.* **16** 11196
[14] Eisenberg I, Caycedo-Soler F, Harris D, Yochelis S, Huelga S F, Plenio M B, Adir N, Keren N and Paltiel Y 2017 *J. Phys. Chem.* B **121** 1240
[15] Eyal L B *et al* 2017 *Proc. Natl Acad. Sci. USA* **114** 9481
[16] Craddock T J A, Friesen D, Mane J, Hameroff S and Tuszynski J A 2014 *J. R. Soc. Interface* **11** 20140677
[17] Celardo G L, Angeli M, Kurian P and Craddock T arXiv:1809.03438
[18] Doria S *et al* 2018 *ACS Nano* **12** 4556
[19] Eisele D M *et al* 2009 *Nat. Nanotechnol.* **4** 658
[20] Freyria F S *et al* 2017 *Nano Lett.* **17** 7665
[21] Chuang C, Kong Lee C, Moix J M, Knoester J and Cao J 2016 *Phys. Rev. Lett.* **116** 196803
[22] Vlaming S M, Bloemsma E A, Linggarsari Nietiadi M and Knoester J 2011 *J. Chem. Phys.* **134** 114507
[23] Didraga C and Knoester J 2004 *J. Chem. Phys.* **121** 10687
[24] Didraga C, Klugkist J A and Knoester J 2002 *J. Phys. Chem.* B **106** 11474

[25] Didraga C and Knoester J 2002 *Chem. Phys.* **275** 307
[26] Fidder H, Knoester J and Wiersma D A 1991 *J. Chem. Phys.* **95** 7880
[27] Moll J, Daehne S, Durrant J R and Wiersma D A 1995 *J. Chem. Phys.* **102** 6362
[28] Monshouwer R, Abrahamsson M, van Mourik F and van Grondelle R 1997 *J. Phys. Chem.* B **101** 7241
[29] Somoza D A, Ke-Wei S, Molina R A and Zhao Y 2017 *PCCP* **19** 25996
[30] Strumpfer J, Sener M and Schulten K 2012 *J. Phys. Chem. Lett.* **3** 536
[31] Lloyd S and Mohseni M 2010 *New J. Phys.* **12** 075020
[32] Higgins K D B, Benjamin S C, Stace T C, Milburn G J, Lovett B W and Gauger E M 2014 *Nat. Commun.* **5** 4705
[33] Celardo G L and Kaplan L 2009 *Phys. Rev.* B **79** 155108
[34] Zhang Y, Celardo G L, Borgonovi F and Kaplan L 2017 *Phys. Rev.* E **96** 052103
[35] Zhang Y, Celardo G L, Borgonovi F and Kaplan L 2017 *Phys. Rev.* E **95** 022122
[36] Giusteri G G, Celardo G L and Borgonovi F 2016 *Phys. Rev.* E **93** 032136
[37] Giusteri G G, Mattiotti F and Celardo G L 2015 *Phys. Rev.* B **91** 094301
[38] Celardo G L, Poli P, Lussardi L and Borgonovi F 2014 *Phys. Rev.* B **90** 085142
[39] Celardo G L, Giusteri G G and Borgonovi F 2014 *Phys. Rev.* B **90** 075113
[40] Celardo G L, Biella A, Kaplan L and Borgonovi F 2013 *Fortschr. Phys.* **61** 250
[41] Scholes G D 2002 *Chem. Phys.* **275** 373
[42] Celardo G L, Borgonovi F, Tsifrinovich V I, Merkli M and Berman G P 2012 *J. Phys. Chem.* C **116** 22105
[43] Ferrari D, Celardo G L, Berman G P, Sayre R T and Borgonovi F 2014 *J. Phys. Chem.* C **118** 20
[44] Dubin F, Melet R, Bariseien T, Grousson R, Legrand L, Schott M and Voliotis V 2006 *Nat. Phys.* **2** 32
[45] Lidzey D G, Bradley D D C, Virgili T, Armitage A, Skolnick M S and Walker S 1999 *Phys. Rev. Lett.* **82** 3316
[46] Clark K A, Krueger E L and Vanden Bout D A 2014 *J. Phys. Chem. Lett.* **5** 2274
[47] Eisele D M *et al* 2014 *Proc. Natl Acad. Sci. USA* **111** E3367
[48] Eisele D M *et al* 2012 *Nat. Chem.* **4** 655
[49] Yuen-Zhou J *et al* 2014 *ACS Nano* **8** 5527
[50] Caram J R *et al* 2016 *Nano Lett.* **16** 6808
[51] Spano F C and Mukamel S 1989 *J. Chem. Phys.* **91** 683
[52] Kassal I, Yuen-Zhou J and Saleh Rahimi-Keshari S 2013 *J. Phys. Chem. Lett.* **4** 362
[53] Ganapathy S *et al* 2009 *Proc. Natl Acad. Sci. USA* **106** 8525
[54] Günther L M, Jendrny M, Bloemsma E A, Tank M, Oostergetel G T, Bryant D A, Knoester J and Köhler J 2016 *J. Phys. Chem.* B **120** 5367
[55] Pšenčík J, Ma Y Z, Arellano J B, Hála J and Gillbro T 2003 *Biophys. J.* **84** 1161
[56] Chew A G M, Frigaard N U and Bryant D A 2007 *J. Bacteriol.* **17** 6176
[57] Linnanto J M and Korppi-Tommola J E I 2014 *J. Phys. Chem.* B **117** 11144
[58] Hohmann-Marriott M F, Blankenship R E and Roberson R W 2005 *Photosyn. Res.* **86** 145
[59] Pšenčík J, Ikonen T P, Laurinmäki P, Merckel M C, Butcher S J, Serimaa R E and Tuma R 2004 *Biophys. J.* **87** 1165
[60] Oostergetel G T, van Amerongen H and Boekema E 2010 *Photosyn. Res.* **104** 245
[61] Prokhorenko V I, Steensgaard D B and Holzwarth A R 2000 *Biophys. J.* **79** 2105
[62] Prokhorenko V I, Steensgaard D B and Holzwarth A R 2003 *Biophys. J.* **85** 3173
[63] Grad J, Hernandez G and Mukamel S 1988 *Phys. Rev.* A **37** 3835
[64] Akkermans E, Gero A and Kaiser R 2008 *Phys. Rev. Lett.* **101** 103602
[65] Gross M and Haroche S 1982 *Phys. Rep.* **93** 301
[66] Strümpfer J and Schulten K 2009 *J. Chem. Phys.* **131** 225101
[67] Damjanović A, Kosztin I, Kleinekathoefer U and Schulten K 2002 *Phys. Rev.* E **65** 031919
[68] Dostál J *et al* 2012 *J. Am. Chem. Soc.* **134** 11611
[69] Didraga C and Knoester J 2004 *J. Chem. Phys.* **121** 946
[70] Saikin S K *et al* 2015 *Sci. Rep.* **4** 9786
[71] Linnanto J M and Korppi-Tommola J E I 2008 *Photosyn. Res.* **96** 227
[72] Anderson P W 1985 *Phys. Rev.* **109** 1492